Constraining the evolution of the north-western margin of Tibet from sedimentary records preserved on the SW margin of the Tarim Basin, and a comparison with the adjacent Pamir.

Shijie Zhang[1,2], Yani Najman[3], Xiumian Hu[2,*], Andrew Carter[4], Chris Mark[5†], Weiwei Xue[2]

1. College of Tourism, Henan Normal University, Xinxiang, China,

2. State Key Laboratory of Mineral Deposit Research, School of Earth Sciences and Engineering, Nanjing University, Nanjing, China,

3. Lancaster Environment Centre, Lancaster University, Bailrigg, UK.

4. School of Natural Sciences, Birkbeck College, London, UK.

5. Department of Geology, Trinity College Dublin, Museum Building, College Green, Dublin, Ireland

* corresponding author, huxm@nju.edu.cn

† now at: Dept of Geosciences, Swedish Museum of Natural History, Stockholm, Sweden.

ABSTRACT

Spatial and temporal variation in Tibetan plateau deformation has important implications for our understanding of crustal deformation processes. The evolution of the NW margin of the plateau and its transition to the Pamir to the west is one under-studied region. We undertook a detrital study, including zircon and apatite fission track analysis and zircon and rutile U-Pb dating, of the most eastern Paleogene sedimentary section studied thus far along the north-western margin of the Tibetan plateau, on the southern margin of the Tarim Basin at Kashitashi. Furthermore, we build on previous work in the most easterly studied Neogene sedimentary section of NW Tibet at Sanju, applying techniques such as apatite fission track analysis, which have not previously been undertaken on this succession. Our data show that an appreciable component of the detrital material in the sedimentary sections was derived from the Songpan-Ganzi – Tianshuihai composite terrane, with some

contribution from the Karakoram and/or the West Qiangtang. Our results clearly indicate a long history of exhumation of the West Kunlun (WKL) since the Triassic; thus in all likelihood the WKL also contributed to our studied successions. However, the WKL signature is not distinctive, and this therefore precludes us from documenting first input of WKL-derived material to the basinal sediments using the techniques we employed. Our thermochronological data record phases of exhumation in the hinterland in the Triassic, Early Cretaceous and Oligo-Miocene. Similar to the Pamir, the Triassic and Oligo-Miocene periods of exhumation are attributed to the Cimmerian and Himalayan orogenies respectively. The Early Cretaceous signal may reflect the distal effects of the Lhasa-Qiangtang collision. Coevality with deformation in Pamir suggests a coupled geodynamic system, with retroarc deformation associated with MeoTethyan subduction in the west, and terrane accretion in the east. The broader extent of deformation in the Pamirs compared to Tibet may then reflect either the effects of slab dynamics, or greater strain partitioning in the east, perhaps due to the broader width of the Gondwanan terranes, along strike differences in the presence of sutures, or crustal heterogeneities.

1 INTRODUCTION

How and when the Tibetan plateau developed has important implications for our understanding of crustal deformation processes. Within this framework, a knowledge of both spatial and temporal variability in deformation is important. For example, North-South variation in the degree of inherited crustal strength resulting from Cretaceous deformation has been proposed to influence the degree and extent of plateau uplift that resulted from Cenozoic India-Asia collision (Ding et al., 2022). Furthermore, the variation in Cretaceous deformation extent and possibly timing between the Pamir and the Kunlun along the northern margin of the Tibetan plateau illustrates East-West variations, the reasons for which are not well known (e.g. Li et al., 2022; Villarreal et al., 2023). Furthermore, the degree of pre-Cenozoic deformation previously underestimated, is being increasingly documented (e.g. Robinson, 2015), impacting estimates of the amount of crustal deformation that must be accounted for in the Cenozoic.

The NW margin of the Tibetan plateau is an understudied region in terms of deformational events, yet it is critical to our understanding: the documented North-South variation in crustal strength resulting from variable Cretaceous deformation as discussed by Ding et al. (2022) (see above) is primarily based on the central-eastern region of Tibet, and the nature of the transition between the Pamir to the west and Tibet to the east (e.g. Villarreal et al. 2023) is lacking in detail. It is therefore to this region that we turn our attention in this paper.

Various provenance and thermochronological arguments have previously been brought to bear on this discussion. In this paper we compare data from within and outwith the Pamir salient, to advance our understanding of the evolution of the NW margin of Tibet. Our approach involves the interrogation of the sedimentary record on the SW margin of the Tarim Basin which abuts the West Kunlun (WKL) northern margin of the plateau (Fig. 1), using various detrital thermochronological and geochronological techniques. We investigate a new Paleogene section at Kashitashi (Fig 1A), which is the most eastern section in NW Tibet studied thus far. Additionally, we build on the previous work of Cao et al. (2015) applying new techniques to the most easterly studied Neogene section at Sanju (Fig 1A), where previously only zircon U-Pb and zircon fission track analyses had been carried out. This approach allows us to complement bedrock studies by sampling a wider catchment area, and to complement modern river detrital studies, by sampling a longer temporal timescale.

2 GEOLOGICAL BACKGROUND

2.1 The geology of NW Tibet and the Pamir

2.1.1. The NW margin of Tibet east of the Pamir Salient, and the Western Tibet plateau.

The Tibetan plateau lies south of the Tarim craton (Fig 1). It is made up of a number of terranes (Fig. 1B) which successively rifted from Gondwana, drifted across the Tethys oceans, and re-assembled along with intraoceanic arcs to eventually form the southern margin of Eurasia by the Late Cretaceous (Metcalfe, 1998; Xiao et al., 2005).

In NW Tibet, furthest north is the West Kunlun (WKL), comprised of North Kunlun and South Kunlun, separated by the Kudi Suture / Tam Karaul Fault. The WKL consists of Precambrian metamorphic basement, Palaeozoic and possible uncommon Mesozoic metasedimentary rocks and Cambrian-Silurian intrusive rocks (Wang et al., 2003; Cao et al., 2015; Zhang et al., 2018 and references therein). The WKL is separated from the terranes to its south by the Karakax Fault. To its south is the composite Songpan-Ganzi – Tianshuihai terrane, consisting of Paleozoic and Mesozoic sedimentary rocks, Cambrian and Triassic plutons and minor Miocene to Quaternary igneous rocks (Deng, 1998; Xiao et al., 2002; Ding et al., 2013). South-east of the Songpan-Ganzi – Tianshuihai terrane, is the Qiangtang terrane, which is comprised of Paleozoic-Mesozoic strata, high-pressure metamorphic mélange, ophiolites, and uncommon Triassic, Cretaceous, and Paleogene intrusive igneous rocks (Wen et al., 2000; Ma et al., 2017). South-west of the Songpan-Ganzi – Tianashuihai terrane is the Karakoram. The Karakoram terrane, considered to be correlative to the Qiangtang (Robinson et al., 2015) comprises Palaeozoic to Mesozoic sedimentary successions, some of which are metamorphosed at some locations (Wen et al., 2000), and Cretaceous and uncommon Paleogene intrusive rocks (Deng, 1998). Neogene intrusive rocks are also found west of the Karakoram Fault (Fraser et al., 2001).

Collision of the North and South Kunlun closed the proto-Tethys in this region in Palaeozoic times (e.g. Xiao et al., 2005). The WKL then represented the southern margin of the Tarim craton of Asia prior to closure of the palaeo-Tethys due to collision with the Qiangtang terrane in the latest Triassic-Early Jurassic Cimmerian orogeny (e.g. Dewey et al., 1988; Ding et al., 2013; Kapp and DeCelles, 2019). The Songpan-Ganzi terrane represents the paleo-accretionary prism which formed between the WKL and the Qiangtang terrane during this ocean closure (Xiao et al., 2005).

Further South, the Lhasa terrane collided with the Qiangtang terrane, debatably sometime between the late Middle Jurassic to Early Cretaceous (e.g. Ma et al., 2017; Raterman et al., 2014; Baxter et al., 2009) closing the Meso-Tethys along the Bangong-Nujung Suture. Finally, the Indian plate collided with the Lhasa terrane in the early Cenozoic, along the Indus-Yarlung suture, closing the Neotethys ocean (e.g. Kapp and DeCelles, 2019; and references therein).

The extent to which the Tibetan plateau deformed and rose in the Mesozoic versus Cenozoic is subject to ongoing revision (e.g. Raterman et al., 2014), with a recent theory being that the two time periods are intrinsically linked in that the uplift of Tibet post India-Asia collision did not occur as a single entity, or progressively, but instead in piece-meal fashion, influenced by inhomogeneities in the crust inherited from variable levels of Cretaceous deformation (Ding et al., 2022).

2.1.2 The Pamir salient

The Pamir salient is, broadly, the western continuation of the NW Tibetan margin (Fig 1B). It is comprised of the North, Central and South Pamir terranes, separated by the Tanymas and Rushan-Pshart sutures, respectively. The North Pamir consists of the Davas-Oytag terrane and the Karakul-Mazar terrane. The North Pamir represents the original Paleozoic southern margin of Asia, with the Davas-Oytag terrane debatably considered to be equivalent to the WKL eastward along strike in NW Tibet, and the Karakul-Mazar terrane equivalent to the Songpan-Ganzi accretionary prism in NW Tibet (Section 2.1.1); the Central and South Pamir are considered to be equivalent to the Qiangtang terrane (Robinson, 2015), although the sutures in the Pamir do not continue eastward into the Qiangtang.

How the Pamir salient developed is a subject of debate. Whilst post-Cimmerian Mesozoic deformation in the Pamir has long been recognised, its extent has been consistently under-estimated in early studies (e.g. see review in Robinson (2015) and its cause ascribed to retroarc deformation associated with subduction of either the Neotethys (e.g. Li et al. 2022) or Mesotethys (e.g. Villarreal et al 2023). Furthermore, whilst pioneering work considered the salient developed from a previously linear east-west trending southern margin of Asia as the result of Cenozoic indentation associated with India-Asia collision (e.g. Burtman and Molnar, 1993), recent work indicates that the protrusion may be the result of an irregular coastline of southern Asia; in the latter scenario infilling of an embayment resulted from juxtaposition of the two adjacent Karakum and Tarim cratons between an intra-oceanic arc (Li et al., 2020; Rembe et al., 2021).

2.2 The sedimentary rocks of the SW Tarim Basin

The Cenozoic stratigraphy of the SW Tarim Basin consists of, from oldest to youngest, the Kashi Group (Aertashi, Qimugen, Kalatar, Wulagen and Bashibulake Formations), Wuqia Group (Keziluoyi, Anjuan and Pakabulake Formations), Atushi Formation and Xiyu Formations (Fig 2). Above the marine Kashi Group, the Wuqia and younger successions are predominantly continental sandstones and mudstones, with conglomerates predominating at the top of the Xiyu Formation. The Wuqia Group is predominantly fluvial, with some lake and swamp facies, whilst the overlying Atushi and Xiyu formations have been interpreted as alluvial fan facies, with some floodplain and aeolian influence (Zheng et al., 2006; Sun and Liu, 2006; Cao et al., 2015; Zheng et al., 2015; Li et al, 2021).

Early work placed the marine Kashi Group as Paleocene to early Oligocene, the Wuqia Group as late Oligocene-Miocene, and the Atushi Formation as Pliocene (e.g. Compiling Group for Xinjiang Regional Stratigraphic Chart 1981; Sun and Liu, 2006; Zheng et al., 2000). More recently, the western Tarim Basin sediments adjacent to the Pamir have been precisely dated, for example the final marine incursion has been biostratigraphically dated at 37-38 Ma (Bosboom et al., 2014) and high resolution magnetostratigraphy has placed the top of the Bashibulake Formation at ~35 Ma, the top of the Wuqia Group at ~23 Ma and the top of the Atushi Formation at 15 Ma at Aertashi (Zheng et al., 2015; see also Blayney et al., 2019). However, lithostratigraphic correlation over long distances is fraught with uncertainty in an active thrust belt setting. With this caveat in mind, we provide below the best age constraints available for our studied Kashitashi and Sanju sections, using published data more proximal to and along strike from our study sites, and augmented by our new data, as described in section 5.1.1 (see below). Furthermore, given this degree of uncertainty, we restrict our depositional age designations to simply “Paleogene” or “Neogene” when used in our later discussion, to avoid over-interpretation of our data.

At our Kashitashi section (Figs. 1C and 2C), the 1:250,000 regional geological map (Shanxi Institute of Geological Survey, 2006) shows the Kashi Group unconformably overlying the Yarkand Group Jurassic strata, and overlain successively by the late Paleogene-early Neogene Wuqia Group and Atushi Formation.

At the Sanju section (Figs. 1D and 2B), Sun and Liu (2006) define the sedimentary succession as consisting of the Pakabulake, Atushi and Xiyu formations, whilst Cao et al. (2015) consider only the Atushi and Xiyu formations to be present. These units are unconformably overlain by the Quaternary Wusu Group.

Whilst the final marine incursion, represented by the Bashibulake Formation of the Kashi Group is dated at 37-38 Ma to the west (Bosboom et al., 2014), further east in the basin at Keliyang and closer to our Kashitashi study site, the final marine retreat occurred at 41 Ma (Bosboom et al., 2014; Sun et al., 2016), and the time equivalent facies to the Bashibulake Formation further west are, in the east, continental. Therefore this formation has been placed above the Kashi Group in the Kekeya section (Fig. 2A) by some workers (Clift et al., 2017; Zheng et al., 2015) and as a non-marine equivalent of the Bashibulake Formation, yet still part of the Kashi Group, by other workers in the region east of Pishan (Compiling Group for Xinjiang Regional Stratigraphic Chart, 1981).

Above the Kashi Group, the Wuqia Group facies are continental, predominantly fluvial, basin-wide. At the Kekeya section to the west of our study areas, magnetostratigraphic data (Zheng et al., 2000), re-correlated with the benefit of a recently discovered tuff layer, has allowed more accurate dating of the continental units (Zheng et al., 2015), further modified in Blayney et al. (2019). According to this revised stratigraphic dating at Kekeya: the Xiyu Formation is dated from either 15 Ma (Zheng et al., 2015) or 20 Ma (Blayney et al., 2019) to top of section at 10 Ma; the Atushi Formation is aged between 20-27 Ma; and the underlying Wuqia Group extends to at least 34 Ma, possibly to >37 Ma, depending on whether the base of the exposed section is considered to be Wuqia Group (Zheng et al., 2000) or Bashibulake Formation (Clift et al., 2017; Zheng et al., 2015 – the Bashibulake is considered to be the base of the exposed section at Kekeya, based on the presence of its muddier facies and evaporites – P. Clift pers comm – since gypsum is typical of the Bashibulake Formation). Note that our new data may indicate that the Anjuan Formation extends into the Neogene (section 5.1.1). The horizontally overlying unconsolidated Wusu Group, is considered to be of Quaternary age (Compiling Group for Xinjiang Regional Stratigraphic Chart, 1981).

3 METHODS

3.1. Rationale and approach.

Previous authors (e.g. Li et al. 2022, Villarreal et al 2023) have commented that post-Cimmerian pre-Cenozoic deformation is located further north (aka north versus south of the Palaeo-Tethyan suture) and may debatably be older in the Pamirs, compared to Tibet. In NW Tibet, the majority of previously published data has been obtained from locations close to the Pamir salient; it is therefore difficult to distinguish between Pamir and Tibet tectonic influences in those regions. We chose the most eastern sedimentary section of the WKL in NW Tibet for our study of Paleogene sedimentary rocks at Kashitashi (fig 1A), as well as adding to data with new analysis types at the previously studied Neogene Sanju section, where only zircon U-Pb and FT analyses had previously been undertaken (Cao et al., 2015). We chose to study Cenozoic detrital sections to get a more comprehensive temporal view compared to modern river sample analyses, and a more comprehensive spatial view compared to bedrock data. We carried out low temperature thermochronological analyses to determine exhumation of the source region, and geochronological analyses to determine provenance in order to determine from what terranes the exhumational data pertained to.

Detrital data from both the Cenozoic sedimentary sections and modern rivers were collected at both locations. The composite Kashitashi section (sections A, B, C, Fig. 1C) was logged and data recorded (Figs 2 and 3), but logging was not required for the Sanju section as this has already been undertaken by previous workers (Sun and Liu, 2006). Data include petrography, zircon and rutile U-Pb age determination, the former also with Hf isotopic characterisation, zircon fission track (ZFT) double dated with U-Pb, and apatite fission track (AFT). Since ZFT double dated with U-Pb data are already available from the Neogene Sanju section (Cao et al., 2015), we utilised these data in our study, rather than replicating analyses. Analyses were carried out at a number of laboratories, and full methodologies are given in Supplementary information S1.

3.2 Petrography

Fourteen sandstones were selected for modal analysis. Approximately 400 points were counted for each sample, following the modified Gazzi-Dickinson method, in which crystal grains larger than 62.5 um within a lithic fragment are counted as monocrystalline grains (Ingersoll et al., 1984).

3.3 Zircon U-Pb

Five samples were analyzed for zircon U-Pb dating. Separated zircon grains were handpicked, mounted in epoxy resin, and polished. Five of the samples were analysed by LA-ICP-MS at the State Key Laboratory of Geological Processes and Mineral Resources, China University of Geosciences, Wuhan. U-Pb analyses were performed using an excimer laser ablation system (GeoLas, 2005) coupled to an Agilent 7500a ICP-MS. Standard 91500 was used as an external standard for U-Pb dating, and Standard GJ-1 was analyzed as the internal standard (Wiedenbeck et al., 1995; Jackson et al., 2004).

Zircon U-Pb dating of the other five samples, which were analysed after fission track dating on the same grains, were analysed by LA-ICP-MS at the State Key Laboratory of Mineral Deposits Research (MiDeR), Nanjing University. Analysis was performed using a New Wave UP193 laser ablation system coupled to an Agilent 7500a ICP-MS. Standard GJ-1 was used as an external standard for U-Pb dating, and zircon standard Mud Tank was analysed as the internal standard (Gain et al., 2019).

3.3 Zircon Hf

In situ zircon Hf isotope analysis of three samples followed U-Pb dating, using a Neptune (Plus) MC-ICP-MS attached to a New Wave ArF 193 nm laser ablation system at the State Key Laboratory of Mineral Deposits Research (MiDeR), Nanjing University. The two zircon reference materials of Mud Tank and 91500 were analysed to correct for instrumental mass bias and depth-dependent inter-element fractionation.

3.4 Rutile U-Pb

Seven samples were analyzed at Trinity College Dublin, Ireland. Rutile grains were mounted in epoxy resin, ground to expose internal surfaces, and polished. Analyses were conducted using a Photon Machines Analyte Excite 193 nm ArF Excimer laser ablation system with a Helex 2-volume ablation cell coupled to an Agilent 7900 quadrupole ICP-MS. Repeated measurements of the primary R10 and the secondary R19, RZ3, PCA-S207, and Sugluk-4 natural rutile standards were used to correct for downhole U-Pb fractionation, mass bias, and intra-session instrument drift (Bracciali et al., 2013; Luvizotto et al., 2009; Shi et al., 2012).

3.5 Fission track

Five apatite separates and five zircon separates were analysed for fission track analysis at University College, London, UK. The separated apatite and zircon grains were mounted in araldite and PTFE respectively, ground to expose internal surfaces, and polished. Then they were etched used 5N HNO^3 at 20°C for 20 s (apatite) and a binary eutectic of KOH:NaOH at 225°C for between 6 and 48 h (zircon) to reveal the spontaneous fission-tracks respectively. Etched grain mounts were packed with mica external detectors and corning glass (CN5 for apatite and CN2 for zircon) dosimeters and irradiated in the FRM 11 thermal neutron facility at the University of Munich in Germany, with fluences of $1.2x10^{16}$ ncm^{-2} (apatite) and $1.25\ x10^{15}$ ncm^{-2} (zircon). Following irradiation the external detectors were etched using 48% HF at 20°C for 25 minutes. Sample ages were determined using the zeta calibration method and IUGS recommended age standards (Hurford, 1990).

4 RESULTS

4.1. Description of the Kashitashi section.

Our new Kashitashi section is a composite of Sections A, B and C as located on Fig 1C and illustrated in Fig 2C. Section A is 600 m thick and is comprised of the uppermost Kashi Group and Keziluoyi Formation. Red coloured thin to thick beds comprise claystone, siltstone and fine sandstone with uncommon medium sandstones and intraformational conglomerate. Section B is 220 m thick and

is comprised of the upper part of the Keziluoyi Formation and Anjuan Formation. Red coloured thin-thick beds are predominantly comprised of siltstone and fine sandstone with less common medium sandstone and claystone. Section C is 300 m thick and is comprised of the Pakabulake Formation. It consists of thin-thick bedded red coloured claystone, siltstone, fine to coarse sandstone and matrix-supported conglomerate with angular to well-rounded clasts up to 15 cm in length. A number of sedimentary structures were observed, as illustrated in Fig. 3.

4.2 Petrography

4.2.1 Conglomerates:

Conglomerates are first recorded at the top of the Kashitashi Section. (Section C; Fig 2 Pakabulake Formation). Clasts are dominated by granite, with subordinate sedimentary (both clastic and carbonate) clasts. By contrast, the conglomerates in the Sanju section are dominated by sandstone clasts. Additionally, limestone clasts are significant in the Atushi Formation conglomerates, whilst schist clasts and a small proportion of granite clasts are recorded in the Xiyu Formation conglomerates (Fig. 2).

4.2.2 Sandstones:

Framework modes (Fig. 4) show that samples are of feldspatho-litho-quartzose, feldspatho-quartzo-lithic and quartzo-lithic in composition (sandstone classification and nomenclature refer to Garzanti (2019)). Samples from Xiyu and Atushi formations in the Sanju section contain less feldspar compared to the Kashitashi region (samples from Keziluoyi, Anjuan and Pakabulake formations) and modern river sands, which include both our own data and published data (Graham et al., 1993; Rittner et al., 2016).

Felsic volcanic fragments dominate the lithic component of the Kashitashi region both in section and in the modern rivers draining into the area predominantly from the South Kunlun (samples 15YK01 and 15YK02, from the Yulongkashi River upstream; Figs. 1, 4 and 5). Sedimentary and metamorphic lithic fragments are more prevalent in the Sanju section and modern rivers which drain more terranes, e.g. both South and North Kunlun (Sanju River, samples SA17 and 55) and include the

Songpan-Ganzi – Tianshuihai terrane (Yulongkashi downstream, sample 50; Kalakashi River, samples 35 and 54; Fig. 1 and 4).

Full petrographic data and thin section photomicrographs are presented in Supplementary Info 3.

4.3 Zircon U-Pb with Hf characterization

Overall, the detrital zircon ages range from 10 Ma to nearly 3000 Ma. All samples from the Sanju and Kashitashi sections have a predominance of grains lying within the range of 200–300 Ma and 400–500 Ma (Fig. 5). The only exception is the modern sand from Sanju River, where the majority of grains lie between 500-600 Ma. In all samples, older grains stretch back to >2000 Ma, with poorly defined greater concentrations between 600-1000 Ma and 1700-2000 Ma. Paleogene grains are sporadically present in both sections. Neogene and Cretaceous grains are also present in the Sanju section. Cretaceous grains are also present in the Sanju modern river sand. Full data are presented in Supplementary Info 4. A comparison of similarity between detrital zircon spectra from samples from the Paleogene and Neogene sections compared to potential source regions is shown in Figure 5.

Of the zircons analyzed for Hf isotopes, only three zircon grains with Paleogene ages were analysed, and they yielded slightly positive εHf(t) values ranging from 0 to +2. The εHf(t) values of Cambrian - Triassic zircons ages range widely but mainly between +10 and -10 (Fig. 6). Full data and plots are presented in Supplementary Info 5.

4.4 Rutile U-Pb

Overall, grains range in age from 10 to >2000 Ma (Fig. 7). All samples from the Kashitashi and Sanju sections, and the Sanju modern river sand, have a major peak between 400-500 Ma. In addition: all formations have appreciable grains extending older to 1000 Ma, except the Xiyu Formation where older grains are rare, and Sanju modern river sand where such grains are absent; grains in the range 100-200 Ma are sporadically recorded; uncommon Cenozoic grains are present in the Sanju section and Sanju modern river sand. Full data are presented in Supplementary Info 6.

4.5 Zircon fission track with U-Pb double dated grains

Data from double-dated zircons from our four new samples from the Wuqia Group of the Kashitashi section and modern river sand from Sanju River were combined with published data from the Sanju section (Cao et al., 2015) in Fig. 8. Following the approach of Cao et al. (2015), a subset of those ZFT data, namely only those grains where the ZFT age is younger than U-Pb age and therefore indicative of an exhumational rather than volcanic ZFT age, were then deconvolved into populations using IsoplotR (Vermeesch, 2018). These are presented as radial plots (Fig. 9). Full data are presented in Supplementary Info 7 and 8. For our new samples, zircons were dominated by old grains with track densities too high to count. Of the populations with countable tracks, the most significant population is broadly of Triassic ZFT age, present in both Kashitashi region, Sanju section, and the modern Sanju River. Only one sample, A2-163 from the Pakabulake Formation, has a Cretaceous signal. Of the Cenozoic populations, Paleocene-Eocene populations are recognised in both sections, whilst late Oligocene-early Miocene populations are only recorded in the Sanju section and modern river, as to be expected given the Paleogene age of the Kashitashi section. The exception to this is sample KE210 from the Kashitash section, which has a dominant Neogene aged population which we interpret as due to late-stage fault activity – see section 5.1.1.

By comparison with U-Pb ages for double dated grains, the grains with Triassic fission track ages are comprised of both a volcanic component with similar U-Pb ages to their FT ages, and a population with older U-Pb ages stretching back to the Precambrian indicating that their corresponding FT ages are of exhumational origin. The one sample with Cretaceous ZFT ages has corresponding volcanic and exhumational grains but the grain number is very small. Considering the Cenozoic grains, in the Paleogene Kashitashi section, the Paleocene signal in sample BK519 is exhumational, but the number of grains in this population is extremely small whilst the Eocene fission track population in sample BK140 is overwhelmingly of volcanic origin. Both exhumational and volcanic Eocene grains are presented in the Neogene Sanju section. Oligocene-Early Miocene fission track populations, only present in the Sanju section, are predominantly exhumational.

4.6 Detrital apatite fission track data

Populations of analysed detrital apatite samples from the sedimentary sections range in FT age between 211 Ma and 24.8 Ma. The modern Yulongkashi River contains a population as young as 5 Ma (Clift et al., 2017) (Fig. 10). The lower number of samples analysed per formation precludes a detailed assessment of trends. Triassic, Cretaceous, Eocene and late Oligocene-early Miocene populations are all represented. Full data are presented in Supplementary Info 9. Without the advantage of double dating, as demonstrated for the zircon fission track data (section 4.5) it is more difficult to differentiate between exhumational and volcanic signals. The radial plots of combined zircon and apatite fission track data shown in Supplementary Info 10 show that there are overlapping apatite and zircon fission track ages for a number of age intervals, suggestive of volcanogenic components if the same source is assumed.

5 INTERPRETATION AND DISCUSSION

5.1 Stratigraphic constraints

5.1.1 Paleogene Kashitashi section

On the basis of the presence of gypsum, typical of the Kashi Group (Bosboom et al., 2014), we consider the base of our Kashitashi Section A (Fig. 2) to be the uppermost part of the Kashi Group, Bashibulake Formation (see section 2.2), in line with the 1:250,000 regional geological map (Shanxi Institute of Geological Survey, 2006). By correlation with the Kekeya section (Cao et al., 2015; Blayney et al., 2019; Fig. 2), and knowledge of the timing of final sea retreat in SW Tarim at Keliyang at 41 Ma (Bosboom et al., 2014; Sun et al., 2016), the Bashibulake Formation can be taken as ranging from 41 Ma at its base to 33-35 Ma at its top. This is consistent with our youngest detrital zircon from the sample of the overlying lowermost Wuqia Group (BK24) dated at 44 Ma, and average weighted mean of the two youngest grains at 45 Ma. Slightly higher up the section, 50 m above the base of the Bashibulake-Wuqia contact, Wuqia Group sample (BK140) records the youngest detrital zircon dated at 41 Ma, and average weighted mean of the five youngest grains at 46.9 Ma. No tighter

356 constraints are provided from zircon U-Pb data up-section, with the youngest grains remaining
357 between 41 Ma and 53 Ma.

358 Rutile and fission track ages provide no further constraint except for sample KE210 from the
359 Anjuan Formation. Sample KE210 has a dominant young ZFT population at 19±2.2 Ma (83.5%). A
360 second aliquot subsequently measured for double dating yielded an age within error at 16.6±1.4 Ma
361 (95%) (Fig. 9) when modelled as a two-component mixture. The double dating shows that this
362 population is exhumational (Fig. 8). If taken at face value, this population would indicate that the
363 upper Kashitashi section extends into the Neogene, at variance with the currently determined age for
364 the Anjuan and Pakabulake Formations as discussed in Section 2.2. As noted in that section,
365 stratigraphic correlation from well dated magnetostratigraphic sections along strike can be difficult in
366 an active tectonic regime; perhaps the stratigraphy does need revision in the light of our new data.
367 However, regarding our new data from Anjuan Formation sample KE210, we note that this Neogene
368 population is not recorded in Anjuan Formation sample KE95 located ca. 100 m stratigraphically
369 below, and it also seems unlikely that evidence of an exhumational event sufficiently significant to
370 dominate the population at >80% would be completely absent by the time of deposition of the
371 overlying Pakabulake Formation (sample A2-163, Fig. 9), and with a Neogene population only being
372 recorded as a subordinate population (12%) in one mid Miocene samples in the Sanju section. We
373 speculate that this population might be the result of partial resetting related to faulting, since the top of
374 section B lies close to a NW-SE trending gully that can be traced on Google Earth for at least 9 km
375 and might be interpreted as a fault since it follows the regional structural trend. More sampling and
376 analysis from the Anjuan Formation at this site will determine whether the depositional age of the
377 formation needs to be refined.

378 5.1.2 Neogene Sanju section

379 At Sanju area, Atushi and Xiyu conglomerates are exposed. This section was originally dated
380 magnetostratigraphically at 2-6.5 Ma (Sun and Liu, 2006). Based on the revised age of the Xiyu
381 Formation at Kekeya (20-<10 Ma) (Zheng et al., 2015), Cao et al. (2015) proposed an older age for

the Sanju section along strike. They used detrital zircons, double dated with U-Pb and FT techniques to demonstrate a volcanic origin, on which they built their correlation. Yet these grains are not from a tuff. They are detrital volcanic-derived gains which make up only a very small proportion of the zircon population, and thus provide maximum depositional ages only; nevertheless, the youngest grains do young up section (from 19 Ma at the base, to 11 Ma at the top) consistent with direct volcanic input. Using the new correlation of Cao et al. (2015), the resulting match with the magnetostratigraphy of Sun and Liu (2006) is poor, but this could be ascribed to the low sampling resolution of the Sanju magnetostratigraphic study. Detrital mineral ages both already published (ZFT from Cao et al., 2015) and our new AFT and rutile data, confirm the Neogene status of the Sanju section but provide no tighter constraint than <19 Ma based on the following observations: ZFT youngest population 19 Ma from sample TSA02, ~810 m above the base of the magnetostratigraphically dated section; a single rutile grain of 22 Ma and youngest AFT population of 25 Ma in sample SZ04 ~24 m above the base of the dated section; a youngest zircon U-Pb dated at 19 Ma in sample TSP01 at the base of the measured section, with the next oldest grain dated at 61 Ma (Fig. 2).

With the caveat that exposure is relatively limited, we located the base of the Atushi conglomerates at Sanju between 250-293 m stratigraphic height below the base of the magnetostratigraphically dated section (N37°10′51.90″, E78°30′8.46″ – location of the lowest Atushi Formation conglomerates, 250 m stratigraphic height below the base of the magnetostratigraphically dated section; N37°10′50.58″, E78°30′05.25″ – location of the uppermost Wuqia Group sandstones, 293 m stratigraphic height below the base of the section, Fig 1D). Therefore, by comparison with the base of the Atushi Formation at the well-dated section at Kekeya (base of Atushi Formation – 27 Ma or 23 Ma, Zheng et al., 2015; Blayney et al. 2019), we broadly agree with the older age assignment of Cao et al. (2015). Yet there remains a mismatch in that if the base of the Sanju conglomerates is taken to be the base of the Atushi Formation (Cao et al., 2015), that is dated at Kekeya at 27-28 Ma or 23 Ma, this conflicts with the youngest U-Pb zircon age providing a maximum depositional age from the base of the Sanju section of 19±0.9 Ma (Cao et al., 2015), albeit only based on one grain, the significance of which is

409 therefore debatable (Dickinson and Gehrels, 2009). Given the likely variability of proximal deposits
410 along strike, we concur that the age of the Sanju conglomerates is broadly early-mid Miocene, but the
411 detail is yet to be resolved.

412 **5.2 Provenance**

413 5.2.1 constraints from zircon data

414 The tectonic terranes of Tibet (section 2.1.1) show variations in zircon U-Pb age signatures,
415 which can be exploited for provenance identification in the basin sediments.

416 Late Paleozoic to Early Mesozoic zircon populations are common throughout the Kashitashi and
417 Sanju sections (Fig. 5, panels 6 and 7), but not in the Sanju modern river sample which drains only the
418 north part of the WKL (Fig. 5, panel 5). Given that Mesozoic plutons are not reported in the WKL
419 hinterland to this study (Fig 1A) and the WKL metasedimentary rocks are predominantly Paleozoic
420 thus providing no Mesozoic zircons (Fig. 5, panel P5), derivation of the Late Paleozoic to Mesozoic
421 detrital zircons in the Cenozoic sections is unlikely to be from the WKL. The most likely, i.e.
422 proximal, source of these zircons is the Songpan-Ganzi – Tianshuihai terrane, where the sedimentary
423 rocks provide Mesozoic detrital zircons, and Triassic igneous rocks crop out (as depicted on Fig 1A)
424 which can account for the younger grains of this Late Paleozoic to Early Mesozoic spectrum (see also
425 Fig 5, panel 4). Close similarity to the Songpan-Ganzi – Tianshuihai terrane is also shown in the
426 MDS plot (Fig 12).

427 A clear difference in signature occurs between the top of the Sanju sedimentary section and the
428 modern Sanju river sample (Fig. 5, panel 5) which drains only the WKL, when the Songpan-Ganzi –
429 Tianshuihai contribution has been cut off. There is no diagnostic signature of the WKL which would
430 allow its detritus to be unambiguously recognised in the sedimentary sections. However, given that
431 the WKL was a topographic feature by the end of the Paleozoic (Cao et al., 2015), contribution to the
432 sedimentary sections is inevitable.

433 Uncommon Mid Cretaceous grains are recorded in the Sanju Section, whilst Paleogene zircons
434 (62-40 Ma) are recorded sporadically throughout the Kashitashi and Sanju sections; double dating
435 with fission track indicates a volcanic source for all of the Paleogene grains in the Paleogene rocks
436 and some of the grains in the Neogene rocks (Fig. 8). Grains of Paleogene age have been documented
437 in the Karakoram and West Qiangtang terranes (Deng, 1998; Chung et al., 2005) and these terranes
438 also make a suitable source for the Cretaceous grains (e.g. Zhuang et al., 2018; Liu et al., 2017; Fig. 5,
439 Panel 3).

440 Neogene zircons of volcanic origin, found only in the Sanju section as expected given the
441 Paleogene depositional age of rocks at Kashitashi, are considered by Cao et al. (2015) to be most
442 likely derived from volcanics of the Songpan-Ganzi – Tianshuihai (Deng, 1998; Li, 2008). The
443 younger Neogene grains may be associated with the airfall volcanic event recorded at ~11 Ma (Li,
444 2008; Zheng et al., 2015).

445 Comparison of the detrital Hf data with bedrock sources (Fig 6) are consistent with the proposal
446 of an input of both Songpan-Ganzi – Tianshuihai and WKL sources, although the 500 Ma zircon
447 population of the modern river draining the WKL (sample SA17) is not well recorded in the source
448 compilation.

449 5.2.2 Constraints to provenance from rutile analyses

450 Our interpretation of rutile provenance is hampered by a paucity of data of the typical rutile
451 signatures of the potential source terranes. The dominant ~400-500 Ma signal in the Kashitashi and
452 Sanju sections is pan-African and likely to be widespread and non-diagnostic. Cenozoic grains,
453 although minor in proportion, may be more distinctive. Rutile is typically a metamorphic mineral
454 (Force, 1980). However, there is only a sparse record (e.g. Zhang et al., 2017) of metamorphism of
455 such age in the WKL, Songpan-Ganzi or Qiangtang terranes in the region, although our sample from
456 the Sanju modern river, which drains the WKL, contains two Cenozoic grains. Cenozoic grains are
457 most likely associated with the widespread Paleogene metamorphism reported from the Karakoram

458 terrane (e.g., Fraser et al., 2001) from which similar mineral cooling ages have been reported (e.g.
459 Zhuang et al., 2018; Clift et al., 2022).

460 5.2.3 Petrography

461 Petrography shows that the Sanju section tends towards a higher proportion of lithic fragments
462 compared to the Kashitashi section, and of these lithics, a higher proportion are metamorphic and
463 sedimentary compared to volcanic (Fig. 4 and Supplementary Info 3). However, it is not possible to
464 ascertain whether this is a temporal or spatial variation, as no older units were analysed from Sanju,
465 and no younger units were deposited at Kashitashi. What can be said is that the hinterland bedrock
466 signature, as defined by modern river data, mimics the sedimentary rock data. The upstream
467 Yulongkashi, which drains into the Kashitashi region, has similar petrography to the Kashitashi
468 sedimentary rock section, whilst the rivers draining to the front (north) of the range, have signatures
469 similar to the Sanju sedimentary rocks. Interestingly, the change in signature between the
470 Yulongkashi upstream (near Kashitashi area) and Yulongkashi downstream (in the Tarim) is similar
471 to the difference in signature between the Kashitashi and Sanju sections.

472 5.2.4 Provenance summary

473 In summary, our data record significant input from the Songpan-Ganzi – Tianshuihai terranes,
474 throughout deposition of the rocks from the Kashitashi and Sanju sedimentary sections. Some
475 contribution from the Karakoram is required to explain the Paleogene rutiles in the Sanju section, and
476 from the Karakoram or Qiantang terranes to explain the Cretaceous zircons in the Sanju section and
477 the Paleogene zircons in the Kashitashi section. The WKL were in all probability also contributing
478 material, as evidenced by the fact that our fission track data from the WKL indicate exhumation since
479 the Triassic (section 5.3.1) and previous research which suggests that, for example, the Tam Karaul
480 Thrust was active since the Mesozoic (e.g. Cowgill, 2001). However, the WKL do not have a
481 diagnostic signature that would allow the first appearance of detritus from these terranes to be
482 detected in the sedimentary record using the techniques we have employed. It should also be noted
483 that some material in our younger samples may be recycled through Cretaceous-Paleogene

sedimentary rocks deposited on the southern margin of the Tarim Basin, that began to be exhumed since the Late Paleogene (e.g. Cheng et al., 2017). However, such deposits, although proximal, are volumetrically relatively minor (Fig 1A).

5.3 Exhumation of the hinterland as determined from thermochronology

Zircon and apatite fission track data are well suited to providing exhumational information in this setting, with double dating of zircons using the U-Pb approach allowing differentiation between volcanic and exhumational ages. We incorporate the previous double dated zircon data from Cao et al. (2015) from the Sanju section, but in contrast to those authors, we do not make interpretations using calculation of lag times, due to the uncertainty in the depositional age of the Sanju section (section 2.2), and we do not combine the data with the Kekeya section data because of this. We also incorporate the AFT data from Clift et al. (2017) from a sample which, according to the GPS location given, is from the Yolungkashi River (37°5.904′ N 79°57.596′ E).

5.3.1 Triassic exhumation

The previously published ZFT data from the Sanju section (Cao et al., 2015) showed a strong Permo-Triassic exhumational event, also now picked out by AFT data from one of our Sanju section samples. (Fig. 12). Our new data from the Paleogene Kashitashi section show a strong Triassic, but not Permian, signature recorded in ZFT although not AFT data (Fig. 12). Some grains must come from the terranes more distal than the WKL in view of their Late Paleozoic to Early Mesozoic U-Pb ages (section 2), and some grains (albeit with ZFT ages in fact of lowermost Jurassic FT age) are from the WKL as such grains are recorded in the Sanju River which only drains the WKL (Fig. 1). The spatial and temporal prevalence of this signal, as well as occurrence of the signal in ZFT data which records exhumation from greater depth compared to exhumation recorded from AFT data, indicates a widespread and significant event. Previous workers have identified and interpreted this event as associated with Paleotethys subduction and final closure during the Cimmerian orogeny (Cao et al., 2015; Li et al., 2019).

5.3.2 Cretaceous exhumation

In our Paleogene Kashitashi section, the Early Cretaceous AFT population is strong in the Kezilouyi Formation and the ZFT signal is strong in the Pakabulake Formation (Fig. 12) where double dating indicates both a volcanic and exhumational component to the ZFT population (Fig. 8). The corresponding zircon U-Pb ages span the Mesozoic to Paleozoic indicating a component of input from terranes more distal than the WKL.

The Cretaceous signal in NW Tibet has previously been interpreted as related to the collision between the Qiangtang and the Lhasa terranes (e.g. Li et al., 2019) or associated with the same event as recorded in the Pamir (Cao et al., 2015) where there was no collision with the Lhasa terrane, and post-Cimmerian deformation is ascribed to retro-arc deformation (Robinson, 2015).

5.3.3 Cenozoic exhumation

Previous work from the NW margin of the plateau shows evidence of exhumation throughout the Cenozoic.

Our data from the Sanju section and modern river concur with and extend previous work. Combining the ZFT data from Cao et al. (2015) with our Sanju modern river ZFT data, and our AFT data from the Sanju section with the modern Yulongkashi AFT data from Clift et al. (2017) (Fig. 12), we observe that an early Miocene ZFT signal is observed in the Neogene Xiyu Formation, and modern river. Furthermore, a late Oligocene to early Miocene AFT signal is present from the Upper Oligocene Artushi Formation, accompanied by a late Miocene signal in the modern river. The double dating from Cao et al. (2015) indicates that the ZFT signal is largely exhumational. We suggest the pattern described above reflects progressive unroofing of the hinterland: shallow unroofing is first recorded by the late Oligocene AFT signature in the Atushi Formation; at that time exhumation was not sufficient to exhume zircon with reset ZFT ages. By Xiyu Formation times, exhumation was sufficiently deep to expose zircons with reset Neogene fission track ages. Progressive exhumation continued as recorded by the late Miocene AFT population in the modern Yulongkashi river, but exhumation is not yet sufficiently deep to record such young ZFT ages in the river, as for example at Sanju. Thus a clear exhumational trend is observed from the Oligo-Miocene times onwards.

536 We note that some of the zircons with Oligo-Miocene FT ages have Triassic U-Pb ages (sample
537 TSX01 and TSA02, Fig. 8), indicating that the Songpan-Ganze – Tianshuihai, and possibly also West
538 Qiangtang, terranes was exhuming during this period. Cao et al. (2015) interpret the Oligo-Miocene
539 zircon fission track population in the Sanju section as derived from the WKL. Likewise, Clift et al.
540 (2017) interpret their Miocene and Pliocene AFT population from the Yulongkashi River as derived
541 from the north Kunlun, from which they calculate exhumation rates of the hinterland by 17 Ma at a
542 rate of ~0.2-0.3mm/yr and by 3.7 Ma at rates of ~0.9-1.3 mm/yr. Taking these grain ages to reflect
543 exhumation (it seems unlikely they are volcanic as that would require erosion from a dominant
544 volcanic source because the lag time precludes direct air fall), we concur with the interpretation of
545 exhumation at this time. However, we do not consider the uplifting region was necessarily the North
546 Kunlun, as they proposed, since their GPS reference shows the sample to be from the upper
547 Yulongkashi River which has its headwaters in the Songpan-Ganzi – Tianshuihai terrane and the river
548 has Triassic detrital zircons which we interpret as Songpan-Ganzi – Tianshuihai -derived (see section
549 2.2, above). By contrast, Triassic plutons are not prevalent in the North Kunlun drainage area of the
550 Yulongkashi River.

551 Nevertheless, ongoing thrusting of the WKL is suggested by: 1) the change in provenance
552 between the top of the Sanju section at 10 Ma, in which detritus from the Songpan-Ganzi –
553 Tianshuihai is still prevalent, and the modern Sanju River in which detritus is solely derived from the
554 WKL (Fig 5); we interpret the change as due to thrust movement beheading the Sanju headwaters that
555 previously delivered Songpan-Ganzi – Tianshuihai detritus to the Sanju section, and 2) first
556 appearance of schists in the conglomerates, ~1240 m up-section from the base of the Xiyu Formation
557 section, most probably derived from the hanging wall of the Tiklik Thrust where such rocks occur
558 (Cheng et al., 2017).

559 Two samples in the Paleogene Kashitashi section have Eocene AFT populations of 53 and 54 Ma
560 which could represent a volcanic or exhumational signal. In the late Oligocene and Neogene Sanju
561 section, there is an AFT signature of 48 Ma, and two samples have a ZFT signature of 50 Ma, of
562 exhumational derivation, and 44 Ma of both exhumational and volcanic origin. The long lag time

between Eocene FT age and Oligocene (Kashitashi section) and Oligo-Miocene (Sanju section) deposition precludes any definitive evidence of rapid exhumation. Li et al. (2019) considered that Eocene exhumation was subdued, limited to localised regions close to faults, and Cao et al. (2015) considered the scattered populations reflected residence in the partial annealing zone prior to exhumation during the Oligo-Miocene event.

5.4 a comparison of Cretaceous deformation between the NW margin of Tibet and the Pamirs.

Post-Cimmerian pre-Himalayan deformation in the Himalayan-Tibet orogen is understudied, increasingly recognised (e.g. Chapman et al 2018), and critical to understanding the degree of geodynamic coupling with the Pamir, as well as to determining both the amount of shortening that needs to be accommodated in the Cenozoic by India-Asia collision, and to better understand how crustal heterogeneities resulting from variations in the extent of Cretaceous deformation may have influenced Cenozoic uplift of the Tibetan plateau (Ding et al., 2022).

Whilst both NW Tibet and the Pamir record the Triassic Cimmerian orogeny and Cenozoic India-Asia collision, Early Cretaceous exhumation differs between the two regions. Both Li et al. (2022) and Villarreal et al. (2023) note that in the Pamirs, Early Cretaceous deformation is significant in the North Pamir, migrating south by the mid Cretaceous. By contrast, in Tibet, significant deformation is largely restricted to the Gondwanan terranes south of the Paleo-Tethyan suture (Ding et al., 2022) although not entirely so (e.g. Li et al., 2019; Liu et al., 2005). However whilst the paper of Li et al (2022) emphasises more of a difference in deformational onset between the Pamir, from 140 Ma, and in Tibet, from 105 Ma, and differences in exhumational causes (Lhasa-Qiangtang collision for Tibet versus retroarc deformation associated with Neotethyan subduction for the Pamirs), Villarreal et al (2023) emphasises more the similarities, with a correlation in timing between Tibet and the Pamir illustrating the geodynamic coupling during Meso-Tethyan subduction, and Lhasa-Qiangtang collision, in the east.

Prior to this current work, data appeared to indicate an abrupt change in the detrital record of Cretaceous exhumation between the Pamir, where Cretaceous cooling ages are common (Fig. 12), and the adjacent NW margin of Tibet (Fig. 12, Panels E and F from Keliyang and Sanju respectively) where there was a near absence of such ages, as also reflected in the paucity of bedrock ages (Li et al., 2019). However, our new data from the Kashitashi section (Fig. 11, panel G) indicates that the previously recorded lack of evidence of Cretaceous deformational signal from the NW margin of Tibet was a data gap rather than being the result of real variation, and the timing of deformation is similar to that of the Pamir (Fig 12 Panel A). In highlighting the similarity in age of Cretaceous deformation between the Pamir and Tibet, our data therefore emphasise the degree of geodynamic coupling proposed by Villarreal et al (2023), with terrane accretion in the east and retroarc deformation in the west, as the Mesotethys subducted. The more restricted extent of Cretaceous deformation in the east likely reflects either slab dynamics in the west, or greater strain partitioning in the east, perhaps related to the narrower width of the Gondwanan terranes in the west, as proposed by Li et al (2022), along strike inhomogeneities in crustal strength as may be caused by the termination of the Tanymas and Rushan-Phart sutures into the Qiantang terrane to the east (Robinson, 2015), or the less rigid nature of the Paleozoic margin of the Asian plate, where the Tarim and Karakum cratons were separated by a Carboniferous intraoceanic arc (Li et al., 2020; Rembe et al., 2021).

6 SUMMARY AND CONCLUSIONS

Our new provenance and low temperature detrital thermochronological data come from 1) the Kashitashi section: the most easterly Paleogene Tarim Basin sedimentary section thus far studied adjacent to the plateau margin in north-west Tibet, and 2) the Sanju section: the previously studied most easterly Neogene sedimentary section abutting the NW margin of Tibet, to which we add lower temperature thermochronological techniques than previously employed.

Our detrital zircon and rutile U-Pb analyses show that the Kashitashi and Sanju sedimentary sections included considerable input from the Songpan-Ganze – Tianshui terrane, with subordinate

input from the Karakoram and possibly the Qiangtang. Input from the WKL was in all probability also significant, since our data show that the area was exhuming since the Triassic. However, first arrival of material from the West Kunlun into the basin is not detectable using the techniques we employed.

Similar to the adjacent Pamirs, our low temperature thermochronological data (apatite and zircon fission track) record exhumational events of the contributing hinterland in the Triassic, late Oligocene to early Miocene onwards, and importantly the Early Cretaceous, where such data were previously sparse to absent in this area. Triassic and Cenozoic exhumational signals reflect the Cimmerian and Himalayan orogenies respectively. The early Cretaceous exhumation in NW Tibet is likely to be associated with the Lhasa-Qiangtang collision. Coevality with the Pamir indicates geodynamic coupling during retroarc deformation associated with Mesotethyan suduction culminating, in the east, with the terrane accretion. The more northern extent of Cretaceous deformation in the Pamir compared to Tibet may reflect slab dynamics in the west, or a higher degree of strain partitioning in the east due to the greater thickness of the Gondwanan terranes, termination of Pamir sutures or crustal heterogeneity on the Asian plate.

ACKNOWLEDGMENTS

This work benefited from discussions with Fin Stuart, Cristina Persano, Ed Sobel, Alex Robinson, Johannes Rembe, Paul Kapp and the assistance of Guillaume Dupont-Nivet, Christopher Kneale and Li Wei in the field. CM thanks David Chew for facilitating access to analytical facilities. We are grateful to reviewers for their constructive suggestions. This work was funded by a Royal Society Newton Fellowship to XH and YN, and the Tethys Major Project (91755209) and International Exchanges Scheme (41511130067) to XH which are funded by the National Natural Science Foundation of China. CM was funded by a Starting Investigator Research Grant from Science Foundation Ireland (18/SIRG/5559).

SUPPORTING INFORMATION

Supplementary Info 1 - Analytical methods

Supplementary Info 2 - Sample information

Supplementary Info 3 – Petrography. 3a: data. 3b: Thin-section microphotographs of sandstones and sands from the Kashitashi and Sanju sections and modern rivers.

Supplementary Info 4 - Zircon U-Pb data

Supplementary Info 5 –Zircon Hf data

Supplementary Info 6 - Rutile U-Pb data

Supplementary Info 7 - ZFT data

Supplementary Info 8 - Zircon U-Pb & ZFT double dating data

Supplementary Info 9- AFT data

Supplementary Info 10 – radial plots combining all data used in Fig 12.

FIGURE CAPTIONS

Fig. 1. A: Simplified geological map of the West Kunlun orogen and adjacent regions, based on Pan et al. (2004). Red stars locate our sedimentary section study areas at Sanju and Kashitashi, red box shows location of Fig. 1C, blue stars show the location of Kekeya and Keliyang sedimentary sections, to which we compare our data. The blue filled circles show the locations of modern river sand petrographic data: Sample 35 is from Rittner et al. (2016; also used for zircon U-Pb data), samples 50, 54, 55 are from Graham et al. (1993) and samples SA17, 15YK01, 15YK02 (the latter two samples also shown on Fig. 1C) are from this study. Blue filled triangle is the location of modern Yulongkashi River sample (AFT data, Clift et al., 2017). Published plutonic zircon U–Pb ages (boxed) are from: 1-Cui et al., 2006; 2-Zhang et al., 2016; 3-Liu et al., 2014; 4-Cui et al., 2007; 5-Ye

et al., 2008; 6-Liu et al., 2015; 7-Wei, 2018. B: Simplified map of major tectonic terranes within the region, modified from Robinson et al. (2007), with location of Fig. 1A shown by box. Red stars show locations of our studied sections at Sanju and Kashitashi (see Fig. 1A), blue stars indicate locations to which we compare our data in Fig 11. C: Simplified geological map of the Kashitashi area, modified after the 1:250,000 regional geological map (Shanxi Institute of Geological Survey, 2006), and located by boxed region in Fig. 1A. Three red lines labelled A, B, C locate our measured sedimentary sections at Kashitashi (Fig. 2C). Blue filled circles locate our modern river samples used for petrographic analysis. Original and revised Formation ages as denoted in the key refer to Compiling Group for Xinjiang Regional Stratigraphic Chart (1981) and this study respectively. D: Simplified geological map of the Sanju area (background image is from Google Earth). The starting point of our measured section is the same as that of Cao et al. (2015) as depicted on the map. Additionally, we explored a further 350 m down-section to define the boundary between the Wuqia Group and Atushi Formation. Filled blue triangles denote our sample sites; filled red circles denote previous sample locations of Cao et al. (2015).

Fig. 2. A: magnetostratigraphically-dated Kekeya section (see Fig. 1A for location) adapted in Blayney et al. (2019) from Zheng et al. (2000, 2015), and reproduced here for reference purposes, to correlate with the Sanju and Kashitashi sections. B: Stratigraphic log and lithostratigraphic divisions of the Sanju section modified from Sun and Liu (2006) and Cao et al. (2015), dated magnetostratigraphically by Sun and Liu (2006), and reinterpreted by Blayney et al. (2019). Sample locations, conglomerate clast counts and maximum depositional age constraints from this study (thermorchronological ages in red text) and from Cao et al. (2015) (in green text), R= MDA based on rutile data, Z = MDA based on zircon data, ZFT = MDA based on zircon fission track data. C: Stratigraphic logs of the Kashitashi sections from this study with sample locations, conglomerate clast counts and maximum depositional age constraints, as constrained by detrital mineral thermochronological ages (red text; Z = MDA based on zircon data). Locations of Sections A, B and C are shown on Fig 1C. Stratigraphic ages of the sections are constrained by the maximum

691 depositional age and comparison with lithostratigraphy in the Kekeya section (Fig 2A). Z. U-Pb,
692 Weighted mean age of youngest detrital zircons where n=>1; R. U-Pb, youngest detrital rutile age;
693 ZFT/AFT, youngest zircon/apatite fission track age peak.

694

695 Fig. 3. Field photographs of representative sedimentary facies. (A) Gypsum layer, Kashi Group,
696 Kashitashi Section A. (B) Mud rip-up clasts and scoured bases, Keziluoyi Formation, Kashitashi
697 Section A. (C) Interbedded sandstone, siltstone and mudstone, Anjuan Formation, Kashitashi Section
698 B. (D) Desiccation cracks Anjuan Formation, Kashitashi Section B. (E) Dwelling burrow, Anjuan
699 Formation, Kashitashi Section B. (F) Incised channel, Pakabulake Formation, Kashitashi Section C.
700 (G) Interbedded conglomerate and sandstone, Atushi Formation, Sanju Section. (H) Siltstone, Xiyu
701 Formation, Sanju Section. (I) Conglomerate, Xiyu Formation, Sanju section. All sedimentary
702 structures are consistent with a continental, predominantly alluvial facies, as interpreted by previous
703 research on these formations (section 2.2).

704

705 Fig. 4. Petrography of sandstones and modern rivers draining from the northern margin of Tibet.
706 A: QFL plot (fields according to the sandstone classification and nomenclature of (Garzanti, 2019))
707 Q= quartz, F= feldspar, L= lithic fragments. B: Lithic fragments plot; Lm = metamorphic lithics, Lv=
708 volcanic lithics, Ls= sedimentary lithics. Samples 15YK01, 15YK02 are modern sands collected from
709 the upper Yulongkashi river, and SA17 was from the Sanju river in this study (see Fig 1A for
710 location). The samples with grey stars are published data. Sample 35 was collected from Kalakashi
711 river (Rittner et al., 2016); samples 50, 54, 55 were collected from Yulongkashi river, Kalakashi river
712 and Sanju river, respectively (Graham et al., 1993). Unlabelled symbols are new data from our
713 sedimentary sections, from formations as denoted in the key. The sample locations are shown in
714 Figure 1.

715

716

Fig. 5. Normalized probability density plots (PDP) with histograms for detrital zircon U-Pb populations from the Kashitashi section, Panel 7 (P7) from this study, and Sanju section, Panel 6 (P6) from Cao et al. (2015), compared to potential source region data:

West Qiangtang (panel 1, P1)- Ding et al. (2013), Gehrels et al. (2011), Pullen et al. (2008), Zhu et al. (2011).

West Songpan-Ganzi - Tianshuihai (Panel 2, P2)-Ding et al. (2013), Hu et al. (2016), Zhang et al. (2017), Dong et al., (2019).

Modern rivers draining Karakoram and South Pamir, representing the potential hinterland provenance of the region west of the Karakoram fault (Panel 3, P3)- Zhuang et al. (2018);

Kalakashi River and Yulongkashi River draining Songpan-Ganzi - Tianshuihai and northern and southern WKL (Panel 4, P4)-Rittner et al. (2016), Clift et al. (2017), Blayney et al. (2019);

Sanju River draining West Kunlun (Panel 5, P5)-this study;

Colours added to aid differentiation of panels (P1-7) as shown on right. Insets show 0-600 Ma sections of the plots in more detail.

Note that where source terrane compilations have relied heavily on detrital zircons of older sedimentary rocks (e.g. West Qiangtang, sedimentary rocks of Jurassic age and older; Songpan-Ganzi – Tianshuihai, sedimentary rocks of Late Triassic age and older), rather than igneous intrusions, younger populations may be under- or unrepresented. This is particularly true of the Songpan-Ganzi – Tianshuihai (P2) where zircons from Mesozoic intrusions are not represented in the compilation based on zircons in sedimentary rocks of Late Triassic age and older.

Fig. 6. A comparison of our new detrital zircon εHf(t) versus U-Pb ages with compiled published data from the West Kunlun, Pamir and Tianshuihai terranes (Zhang et al., 2023).

741 Fig. 7. Detrital rutile U-Pb ages presented as normalized probability density plots with
742 histograms for the modern Sanju river, Sanju Section, and Kashitashi Section (sections A, B and C, as
743 shown on Fig 1C). Insets show the same data, 0-200 Ma, in expanded form.

744

745 Fig. 8. Fission-track versus U–Pb ages for double-dated single zircon grains from samples from
746 Kashitashi and Sanju sections. Three grains (in samples KE210 and BK140) have ZFT ages older than
747 their corresponding U–Pb ages at 1σ but lie on the 1:1 line at 2σ error, and are therefore not excluded
748 from the plot. Samples with symbol * from the Sanju section are from Cao et al. (2015).

749

750 Fig. 9. Radial plots showing a subset of the zircon fission track data shown in Fig 7 interpreted
751 as representing exhumational signals. There is a considerable population of zircons with fission tracks
752 too numerous to count in all samples. These cannot be represented on the radial plots. Samples from
753 the Kashitashi section and the modern river at Sanju are from this study, and those from the Sanju
754 section (symbol*) are from Cao et al. (2015). Using the same approach as Cao et al. (2015), the radial
755 plots only include zircon grains for which ZFT ages are younger than the corresponding U-Pb ages,
756 thereby excluding volcanic zircons. Samples KE95 and KE210 aliquot 1 (symbols #) do not have
757 corresponding U-Pb data and therefore all grains are plotted. The Eocene population in sample BK140
758 (included as Peak 1 in bracketed italics, superscript[1]) is required to be included in this exhumational
759 plot because it meets the criteria in that a few grains in the population have ZFT ages younger than U-
760 Pb age. However, the ZFT ages of these grains are only slightly younger than U-Pb age, and the
761 majority of the grains in this population are volcanic (ZFT and U-Pb age within error). Therefore in
762 all likelihood these grains are also volcanic.

763

764 Fig. 10. Radial plots showing the distribution of detrital apatite fission track ages, in samples
765 from the Sanju section and Kashitashi section (sections A and C, see Fig 1C for location). Sample
766 with symbol * is from the modern sand of the Yulongkashi river from Clift et al. (2017).

Fig. 11. Multidimensional Scaling (MDS) Plot (Vermeesch, 2013) based on calculated K–S distances between zircon U–Pb age spectra, comparing Paleogene samples from Kashitashi section and Neogene samples from Sanju section, with potentially contributing hinterland source regions (West Kunlun (WKL, as characterised by modern Sanju River sand sample SA17), West Qiangtang, West Songpan-Ganzi – Tiasnhuihai and the region west of the Karakoram fault (Karakoram and South Pamir), and the Karakoram as detailed in Fig 5. References as for Fig 5, with bedrock Karakoram data from Zhuang et al., (2016) and references therein.

Fig. 12. A summary of new and published detrital zircon and apatite FT ages along strike from the Pamir to NW Tibet: From West to East: West Pamir (Panel A), data from Carrapa et al. (2014), Chapman et al. (2020) and Li et al. (2023); Northeast Pamir (Panel B), data from Carrapa et al. (2014); Aertashi section (Panel C, data from Blayney et al. (2019); Kekeya Section (Panel D), data from Cao et al. (2015); Keliyang Section (Panel E), data from Wang et al. (2021); Sanju section (Panel F), zircon FT data from Cao et al. (2015), apatite FT data from this study; Kashitashi section (Panel G), data from this study. For ZFT data from this study, only populations detected as exhumational in origin on account of their ZFT ages being younger than U-Pb ages are included, except for the Yulongkashi River samples (13062401, Clift et al., 2017) and KE95 where double-dating was not undertaken. Sample KE210 was not included in this figure because we interpret the ages as due to resetting by local fault reactivation as described in section 5.1.1. The Eocene ZFT population in sample BK140 (as shown by an asterisk) consists of 3 grains that narrowly fall off the 1:1 line (Fig. 8), in amongst a total population of 6 grains in this aged population, which fall on the 1:1 line, and are thus interpreted as of volcanic origin. Thus the 3 grains in the population in this figure, may also be recording a volcanic rather than exhumational signal. These data are also displayed as radial plots in Supplementary Item 10.

REFERENCES CITED

Baxter, A. T., Aitchison, J. C., & Zyabrev, S. V. (2009). Radiolarian age constraints on Mesotethyan ocean evolution, and their implications for development of the Bangong–Nujiang suture, Tibet. Journal of the Geological Society, 166(4), 689-694. https://doi.org/10.1144/0016-76492008-128

Blayney, T., Dupont-Nivet, G., Najman, Y., Proust, J.N., Meijer, N., Roperch, P., Sobel, E.R., Millar, I., & Guo, Z. (2019). Tectonic evolution of the Pamir recorded in the western Tarim Basin (China): sedimentologic and magnetostratigraphic analyses of the Aertashi section. Tectonics, 38 (2), 492-515. https://doi.org/10.1029/2018TC005146

Bosboom, R., Dupont-Nivet, G., Grothe, A., Brinkhuis, H., Villa, G., Mandic, O., Stoica, M., Kouwenhoven, T., Huang, W.T., Yang, W., & Guo, Z.J. (2014). Timing, cause and impact of the late Eocene stepwise sea retreat from the Tarim Basin (west China). Palaeogeography Palaeoclimatology Palaeoecology, 403, 101-118. https://doi.org/10.1016/j.palaeo.2014.03.035

Bracciali, L., Parrish, R.R., Horstwood, M.S., Condon, D.J., & Najman, Y. (2013). UPb LA-(MC)-ICP-MS dating of rutile: New reference materials and applications to sedimentary provenance. Chemical Geology, 347, 82-101. https://doi.org/10.1016/j.chemgeo.2013.03.013

Cao, K., Wang, G.-C., Bernet, M., van der Beek, P., & Zhang, K.-X. (2015) Exhumation history of the West Kunlun Mountains, northwestern Tibet: Evidence for a long-lived, rejuvenated orogen. Earth and Planetary Science Letters, 432, 391-403. https://doi.org/10.1016/j.epsl.2015.10.033

Carrapa, B., Mustapha, F. S., Cosca, M., Gehrels, G., Schoenbohm, L. M., Sobel, E. R., DeCelles, P. G., Russell, J., & Goodman, P. (2014). Multisystem dating of modern river detritus from Tajikistan and China: Implications for crustal evolution and exhumation of the Pamir. Lithosphere, 6, 443– 455. https://doi.org/10.1130/L360.1

Chapman, J. B., Carrapa, B., DeCelles, P. G., Worthington, J., Mancin, N., Cobianchi, M., Stoica, M., Wang, X., Gadoev, M., & Oimahmadov, I. (2020). The Tajik Basin: A composite record of sedimentary basin evolution in response to tectonics in the Pamir. Basin Research, 32(3), 525–545. https://doi.org/10.1111/bre.12381

Cheng, X., Chen, H., Lin, X., Wu, L., & Gong, J. 2017, Geometry and Kinematic Evolution of the Hotan-Tiklik Segment of the Western Kunlun Thrust Belt: Constrained by Structural Analyses

822 and Apatite Fission Track Thermochronology. The Journal of Geology, 125(1), 65-82.
823 https://doi.org/10.1086/689187
824 Chung, S.L., Chu, M.F., Zhang, Y., Xie, Y., Lo, C.H., Lee, T.Y., Lan, C.Y., Li, X., Zhang, Q., &
825 Wang, Y. (2005). Tibetan tectonic evolution inferred from spatial and temporal variations in
826 post-collisional magmatism. Earth Science Reviews, 68(3-4), 173-196.
827 https://doi.org/10.1016/j.earscirev.2004.05.001
828 Clift, P. D., Mark, C., Alizai, A., Khan, H., & Jan, M. Q. (2022). Detrital U–Pb rutile and zircon data
829 show Indus River sediment dominantly eroded from East Karakoram, not Nanga Parbat. Earth
830 and Planetary Science Letters, 600, 117873. https://doi.org/10.1016/j.epsl.2022.117873
831 Clift, P.D., Zheng, H., Carter, A., Böning, P., Jonell, T.N., Schorr, H., Shan, X., Pahnke, K., Wei, X.,
832 & Rittenour, T. (2017). Controls on erosion in the western Tarim Basin: Implications for the
833 uplift of northwest Tibet and the Pamir. Geosphere, 13(5), 1747-1765.
834 https://doi.org/10.1130/GES01378.1
835 Compiling Group for Xinjiang Regional Stratigraphic Chart. (1981). Regional Stratigraphic Chart of
836 Northwestern China, Branch of Xinjiang Uygur Autonomous Region. Geological Publishing
837 House, Beijing (in Chinese), 346-402.
838 Cowgill, E. (2001). Tectonic evolution of the Altyn Tagh – Westerm Kunlun Fault System,
839 Northwestern China. Unpublished PhD thesis, UCLA, USA.
840 Cui, J.T., Wang, J.C., Bian, X.W., Luo, Q.Z., Zhu, H.P., Wang, M.C., Chen, G.C. (2007). Zircon
841 SHRIMP U-Pb dating of the Dongbake gneissic tonalite in northern Kangxiwar, West Kunlun:
842 Geological Bulletin of China, 26(6), 726-729.
843 Cui, J.T., Wang, J.C., Bian, X.W., Zhu, H.P. (2006). Geological characteristics of Early Paleozoic
844 amphibolite and tonalite in northern Kangxiwar, West Kunlun, China and their zircon SHRIMP
845 U-Pb dating: Geological Bulletin of China, 25(12), 1450-1457.
846 Deng, W.M. (1998). Cenozoic Intraplate Volcanic Rocks in the Northern Qinghai-Xizang Plateau.
847 Geological Publishing House, Beijing, 19-26.

Dewey, J. F., Shackleton, R. M., Chengfa, C., & Yiyin, S. (1988). The tectonic evolution of the Tibetan Plateau. Philosophical Transactions of the Royal Society of London. Series A, Mathematical and Physical Sciences, 327(1594), 379-413. https://doi.org/10.1098/rsta.1988.0135

Dickinson, W.R., & Gehrels, G.E. (2009). Use of U–Pb ages of detrital zircons to infer maximum depositional ages of strata: a test against a Colorado Plateau Mesozoic database. Earth and Planetary Science Letters, 288(1-2), 115-125. https://doi.org/10.1016/j.epsl.2009.09.013

Ding, L., Kapp, P., Cai, F., Garzione, C. N., Xiong, Z., Wang, H., & Wang, C. (2022). Timing and mechanisms of Tibetan Plateau uplift. Nature Reviews Earth & Environment, 3(10): 652-667. https://doi.org/10.1038/s43017-022-00318-4

Ding, L., Yang, D., Cai, F.L., Pullen, A., Kapp, P., Gehrels, G.E., Zhang, L.Y., Zhang, Q.H., Lai, Q.Z., & Yue, Y.H. (2013). Provenance analysis of the Mesozoic Hoh-Xil-Songpan-Ganzi turbidites in northern Tibet: Implications for the tectonic evolution of the eastern Paleo-Tethys Ocean. Tectonics, 32(1), 34-48. https://doi.org/10.1002/tect.20013

Dong, R., Wang, H., Yan, Q. H., Zhang, X. Y., Wei, X. P., Li, P., & Zhou, K. L. (2019). Geochemical Characteristics and Zircon U-Pb Ages of the Bayankalashan Group in the Tianshihai Terrain of the West Kunlun Orogenic Belt: Implication for its Provenance and Tectonic Environment. Geotecton. Metallog, 43, 1236-1257.

Fraser, J.E., Searle, M.P., Parrish, R.R., and Noble, S.R. (2001). Chronology of deformation, metamorphism, and magmatism in the southern Karakoram Mountains: Geological Society of America Bulletin. 113(11) 1443-1455. https://doi.org/10.1130/0016-7606(2001)113<1443:CODMAM>2.0.CO;2

Gain, S. E., Gréau, Y., Henry, H., Belousova, E., Dainis, I., Griffin, W. L., & O'reilly, S. Y. (2019). Mud Tank Zircon: Long-term evaluation of a reference material for U-Pb dating, Hf-isotope analysis and trace element analysis. Geostandards and Geoanalytical Research, 43(3), 339-354. https://doi.org/10.1111/ggr.12265

Garzanti, E. (2019). Petrographic classification of sand and sandstone. Earth-science reviews, 192(545-563). https://doi.org/10.1016/j.earscirev.2018.12.014

875 Gehrels, G., Kapp, P., Decelles, P., Pullen, A., Blakey, R., Weislogel, A., Ding, L., Guynn, J., Martin,
876 A., Mcquarrie, N., & Yin, A. (2011). Detrital zircon geochronology of pre-Tertiary strata in the
877 Tibetan–Himalayan orogen. Tectonics, TC5016(30), 5. https://doi.org/10.1029/2011TC002868
878 Graham, S., Hendrix, M., Wang, L., and Carroll, A. (1993). Collisional successor basins of western
879 China: Impact of tectonic inheritance on sand composition. Geological Society of America
880 Bulletin, 105(3), 323-344, https://doi.org/10.1130/0016-
881 7606(1993)105<0323:CSBOWC>2.3.CO;2
882 Hu, J., Wang, H., Huang, C., Tong, L., Mu, S., & Qiu, Z. (2016). Geological characteristics and age
883 of the Dahongliutan Fe-ore deposit in the Western Kunlun orogenic belt, Xinjiang, northwestern
884 China. Journal of Asian Earth Sciences, 116, 1-25. https://doi.org/10.1016/j.jseaes.2015.08.014
885 Hurford, A.J. (1990). Standardization of fission track dating calibration: Recommendation by the
886 Fission Track Working Group of the IUGS Subcommission on Geochronology. Chemical
887 Geology, Isotope Geoscience Section, 80(2), 171-178. https://doi.org/10.1016/0168-
888 9622(90)90025-8
889 Ingersoll, R.V., Bullard, T.F., Ford, R.L., Grimm, J.P., Pickle, J.D., & Sares, S.W. (1984). The effect
890 of grain size on detrital modes: a test of the Gazzi-Dickinson point-counting method. Journal of
891 Sedimentary Research, 54(1), 103-116. https://doi.org/10.1306/212F83B9-2B24-11D7-
892 8648000102C1865D
893 Jackson, S.E., Pearson, N.J., Griffin, W.L., & Belousova, E.A. (2004). The application of laser
894 ablation-inductively coupled plasma-mass spectrometry to in situ U–Pb zircon geochronology.
895 Chemical Geology, 211(1-2), 47–69. https://doi.org/10.1016/j.chemgeo.2004.06.017
896 Kapp, P., & DeCelles, P. G. (2019). Mesozoic–Cenozoic geological evolution of the Himalayan-
897 Tibetan orogen and working tectonic hypotheses. American Journal of Science, 319(3), 159-254.
898 https://doi.org/10.2475/03.2019.01
899 Li, G., Sandiford, M., Fang, A., Kohn, B., Sandiford, D., Fu, B., Zhang, T., Cao, Y., & Chen, F.
900 (2019). Multi-stage exhumation history of the West Kunlun orogen and the amalgamation of the
901 Tibetan Plateau. Earth and Planetary Science Letters, 528, 115833.
902 https://doi.org/10.1016/j.epsl.2019.115833

Li, L., Najman, Y., Dupont-Nivet, G., Parra, M., Roperch, P., Kaya, M., Meijer, N., O'Sullivan, P., Jepson, G., & Aminov, J. (2023). Mesozoic–Cenozoic multistage tectonic evolution of the Pamir: Detrital fission-track constraints from the Tajik Basin. Basin Research, 35(2), 530-550. https://doi.org/10.1111/bre.12721

Li, Y. P., Robinson, A. C., Gadoev, M., & Oimuhammadzoda, I. (2020). Was the Pamir salient built along a Late Paleozoic embayment on the southern Asian margin? Earth and Planetary Science Letters, 550, 116554. https://doi.org/10.1016/j.epsl.2020.116554

Li, Y. P., Robinson, A. C., Zucali, M., Gadoev, M., Oimuhammadzoda, I., Lapen, T. J., & Carrapa, B. (2022). Mesozoic Tectonic Evolution in the Kurgovat‐Vanch Complex, NW Pamir. Tectonics, 41(10), e2021TC007180. https://doi.org/10.1029/2021TC007180

Liu, D., Shi, R., Ding, L., Huang, Q., Zhang, X., Yue, Y., & Zhang, L. (2017). Zircon U–Pb age and Hf isotopic compositions of Mesozoic granitoids in southern Qiangtang, Tibet: implications for the subduction of the Bangong–Nujiang Tethyan Ocean. Gondwana Research, 41, 157-172. https://doi.org/10.1016/j.gr.2015.04.007

Liu, Z., Jiang, Y.H., Jia, R.Y., Zhao, P., & Zhou, Q. (2015). Origin of Late Triassic high-K calc-alkaline granitoids and their potassic microgranular enclaves from the western Tibet Plateau, northwest China: Implications for Paleo-Tethys evolution. Gondwana Research, 27(1), 326-341. https://doi.org/10.1016/j.gr.2013.09.022

Liu, Z., Jiang, Y.H., Jia, R.Y., Zhao, P., Zhou, Q., Wang, G.C., & Ni, C.Y. (2014). Origin of Middle Cambrian and Late Silurian potassic granitoids from the western Kunlun orogen, northwest China: a magmatic response to the Proto-Tethys evolution. Mineralogy and Petrology, 108, 91–110. https://doi.org/10.1007/s00710-013-0288-0

Luvizotto, G., Zack, T., Meyer, H., Ludwig, T., Triebold, S., Kronz, A., Münker, C., Stockli, D., Prowatke, S., & Klemme, S. (2009). Rutile crystals as potential trace element and isotope mineral standards for microanalysis. Chemical Geology, 261(3-4), 346-369. https://doi.org/10.1016/j.chemgeo.2008.04.012

929 Ma, A., Hu, X., Garzanti, E., Han, Z., & Lai, W. (2017). Sedimentary and tectonic evolution of the
930 southern Qiangtang basin: implications for the Lhasa-Qiangtang collision timing. Journal of
931 Geophysical Research: Solid Earth, 122, (7), 4790-4813. https://doi.org/10.1002/2017JB014211
932 Metcalfe, I. (1998). Palaeozoic and Mesozoic geological evolution of the SE Asian region:
933 multidisciplinary constraints and implications for biogeography. Biogeography and geological
934 evolution of SE Asia, 25-41.
935 Pan, G., Ding, J., Yao, D., & Wang, L. (2004). Geological map of the Qinghai-Xizang (Tibet) Plateau
936 and adjacent areas, with guidebook. Chengdu, China, Cartographic Publishing House.
937 Pullen, A., Kapp, P., Gehrels, G.E., Vervoort, J.D., & Ding, L. (2008). Triassic continental subduction
938 in central Tibet and Mediterranean-style closure of the Paleo-Tethys Ocean. Geology, 36(5),
939 351–354. https://doi.org/10.1130/G24435A.1
940 Raterman, N. S., Robinson, A. C., & Cowgill, E. S. (2014). Structure and detrital zircon
941 geochronology of the Domar fold-thrust belt: Evidence of pre-Cenozoic crustal thickening of the
942 western Tibetan Plateau. Geological Society of America Special Papers, 507, 89-104.
943 https://doi.org/10.1130/2014.2507(05)
944 Rittner, M., Vermeesch, P., Carter, A., Bird, A., Stevens, T., Garzanti, E., Andò, S., Vezzoli, G., Dutt,
945 R., & Xu, Z. (2016). The provenance of Taklamakan desert sand. Earth and Planetary Science
946 Letters, 437, 127–137. https://doi.org/10.1016/j.epsl.2015.12.036
947 Robinson, A. C. (2015). Mesozoic tectonics of the Gondwanan terranes of the Pamir plateau. Journal
948 of Asian Earth Sciences, 102, 170-179. https://doi.org/10.1016/j.jseaes.2014.09.012
949 Shanxi institute of geological survey. (2006). The 1:250,000 regional geological map in Qiaha area,
950 P.R.C. Beijing, Geological Press.
951 Shi, G., Li, X., Li, Q., Chen, Z., Deng, J., Liu, Y., Kang, Z., Pang, E., Xu, Y., & Jia, X. (2012). Ion
952 microprobe U-Pb age and Zr-in-rutile thermometry of rutiles from the Daixian rutile deposit in
953 the Hengshan Mountains, Shanxi Province, China. Economic Geology, 107(3), 525–535.
954 https://doi.org/10.2113/econgeo.107.3.525
955 Sun, J.M., & Liu, T.S. (2006). The age of the Taklimakan Desert. Science, 312, 5780, 1621.
956 https://doi.org/10.1126/science.1124616

Sun, J.M., Windley, B.F., Zhang, Z.L., Fu, B.H., & Li, S.H. (2016). Diachronous seawater retreat from the southwestern margin of the Tarim Basin in the late Eocene. Journal of Asian Earth Sciences, 116, 222–231. http://dx.doi.org/10.1016/j.jseaes.2015.11.020

Vermeesch, P. (2013). Multi-sample comparison of detrital age distributions. Chemical Geology, 341(2), 140–146. https://doi.org/10.1016/j.chemgeo.2013.01.010

Vermeesch, P. (2018). IsoplotR: A free and open toolbox for geochronology. Geoscience Frontiers, 9(5), 1479–1493. https://doi.org/10.1016/j.gsf.2018.04.001

Villarreal, D. P., Robinson, A. C., Chapman, J. B., Carrapa, B., Oimuhammadzoda, I., Gadoev, M., & Li, Y. (2023). Early Cretaceous displacement on the Tanymas thrust fault, Northern Pamir, Tajikistan, and regional tectonic implications. Journal of Asian Earth Sciences: X, 9, 100147. https://doi.org/10.1016/j.jaesx.2023.100147

Wang, E., Wan, J., & Liu, J. (2003). Late Cenozoic geological evolution of the foreland basin bordering the West Kunlun range in Pulu area: Constraints on timing of uplift of northern margin of the Tibetan Plateau. Journal of Geophysical Research: Solid Earth, 108, B8. https://doi.org/10.1029/2002JB001877

Wang, P., Liu, D., Li, H., Chevalier, M., Wang, Y., Pan, J., Zheng, Y., Ge, C., Bai, M., & Wang, S. (2021). Sedimentary provenance changes constrain the Eocene initial uplift of the Central Pamir, NW Tibetan Plateau. Frontiers in Earth Science, 9, 741194. https://doi.org/10.3389/feart.2021.741194

Wei, X. P. (2018). Spatial-temporal Pattern, Petrogenesis and Tectonic Implications of the Triassic Granitoids from the Western Kunlun Orogen，Northwestern China. PhD. thesis, Guangzhou Institute of Geochemistry, Chinese Academy of Sciences, Guangzhou.

Wen, S., Sun, D., Yin, J., Chen, T., & Luo, H. (2000). Chapter 2: Stratigraphy. The Geological Formation and Evolution of the Karakorum and Kunlun Mountains. Chinese Science Publishing House, Beijing, 6–92.

Wiedenbeck, M. A., Alle, P. C., Corfu, P., Griffin, F., Meier, W. L., Oberli, M., Quadt, F. V., Roddick, J.C., & Spiegel, W. (1995). Three natural zircon standards for U-Th-Pb, Lu-Hf, trace

element and REE analyses. Geostandards newsletter, 19(1), 1–23. https://doi.org/10.1111/j.1751-908X.1995.tb00147.x

Xiao, W.J., Windley, B.F., Chen, H.L., Zhang, G.C., & Li, J.L. (2002). Carboniferous-Triassic subduction and accretion in the western Kunlun, China: Implications for the collisional and accretionary tectonics of the northern Tibetan Plateau. Geology, 30(4), 295–298. https://doi.org/10.1130/0091-7613(2002)030<0295:CTSAAI>2.0.CO;2

Xiao, W. J., Windley, B. F., Liu, D. Y., Jian, P., Liu, C. Z., Yuan, C., & Sun, M. (2005). Accretionary tectonics of the Western Kunlun Orogen, China: a Paleozoic–Early Mesozoic, long-lived active continental margin with implications for the growth of Southern Eurasia. The Journal of Geology, 113(6), 687-705. https://doi.org/10.1086/449326

Ye, H.M., Li, X.H., Li, Z.X., & Zhang, C.L. (2008). Age and origin of high Ba–Sr appinite–granites at the northwestern margin of the Tibet Plateau: Implications for early Paleozoic tectonic evolution of the Western Kunlun orogenic belt. Gondwana Research, 13, 126-138. https://doi.org/ 10.1016/j.gr.2007.08.005

Zhang, C.L., Zou, H.B., Ye, X.T., & Chen, X.Y. (2018). Tectonic evolution of the West Kunlun Orogenic Belt along the northern margin of the Tibetan Plateau: Implications for the assembly of the Tarim terrane to Gondwana. Geoscience Frontiers, 10(3), 973–988. https://doi.org/10.1016/j.gsf.2018.05.006

Zhang, L., Long, X., Zhang R., Dong, Y., Yuan, C., Xiao, W., & Wang Y. (2017). Source characteristics and provenance of metasedimentary rocks from the Kangxiwa Group in the Western Kunlun Orogenic Belt, NW China: Implications for tectonic setting and crustal growth. Gondwana Research, 46, 43–56. http://dx.doi.org/10.1016/j.gr.2017.02.014

Zhang, S., Hu, X., Zhang, J., Li, Q., Xu, Y., Yu, Y., & Han, L. (2023). A database of detrital zircon U–Pb ages and Hf isotopic compositions from the Tarim, West Kunlun, Pamir, Tajik and Tianshuihai terranes. Geoscience Data Journal. Early View. https://doi.org/10.1002/gdj3.213

Zhang, Y., Niu, Y., Hu, Y., Liu, J., Ye, L., Kong, J., & Duan, M. (2016). The syncollisional granitoid magmatism and continental crust growth in the West Kunlun Orogen, China – Evidence from

geochronology and geochemistry of the Arkarz pluton. Lithos, 245, 191–204. https://doi.org/10.1016/j.lithos.2015.05.007

Zheng, H., Mcaulay Powell, C., An, Z., Zhou, J., & Dong, G. (2000). Pliocene uplift of the northern Tibetan Plateau. Geology, 28(8), 715–718. https://doi.org/10.1130/0091-7613(2000)28<715:PUOTNT>2.0.CO;2

Zheng, H., Wei, X., Tada, R., Clift, P.D., Wang, B., Jourdan, F., Wang, P., & He, M. (2015). Late Oligocene-early Miocene birth of the Taklimakan Desert. Proceedings of the National Academy of Sciences, 112, 7662–7667.

Zheng, H.B., Huang, X.T., & Butcher, K. (2006). Lithostratigraphy, petrography and facies analysis of the Late Cenozoic sediments in the foreland basin of the West Kunlun. Palaeogeography Palaeoclimatology Palaeoecology, 241(1), 61–78. https://doi.org/10.1016/j.palaeo.2006.06.015

Zhu, D.C., Zhao, Z.D., Niu, Y., Dilek, Y., & Mo, X.X. (2011). Lhasa terrane in southern Tibet came from Australia. Geology, 39(8), 727–730. https://doi.org/10.1130/G31895.1

Zhuang, G., Najman, Y., Tian, Y., Carter, A., Gemignani, L., Wijbrans, J., Jan, M.Q., & Khan, M.A. (2018). Insights into the evolution of the Hindu Kush–Kohistan–Karakoram from modern river sand detrital geo-and thermochronological studies. Journal of the Geological Society, 175(6), 934–948. https://doi.org/10.1144/jgs2018-007

Fig. 1

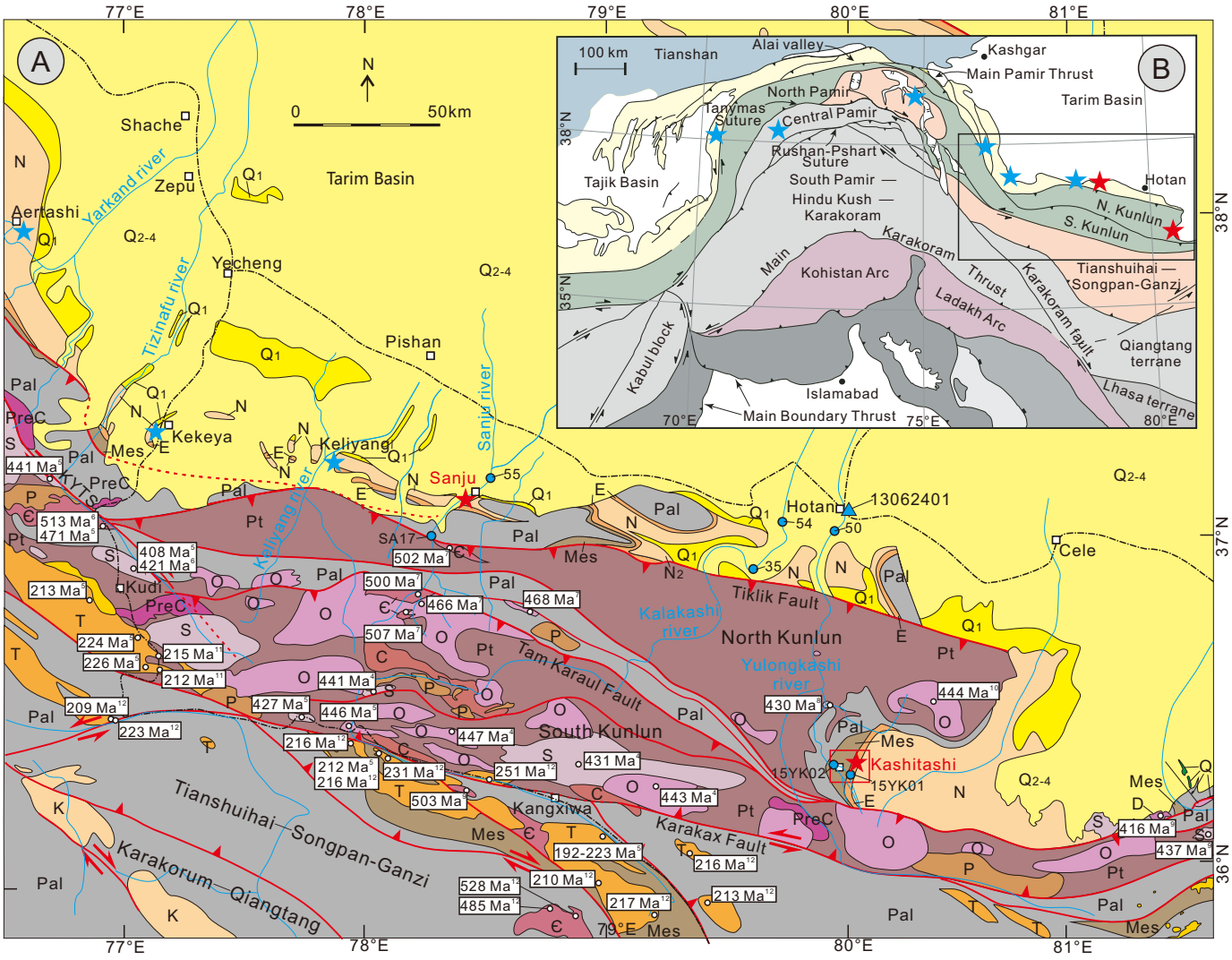
A
B
C
D
77°E
78°E
79°E
80°E
81°E
38°N
37°N
36°N
N
0
50km
Shache
Yarkand river
Zepu
Tarim Basin
Aertashi
Yecheng
Tizinafu river
Pishan
Sanju river
Kekeya
Keliyang
Kelilyang river
Sanju
Kudi
Hotan
13062401
Cele
Tiklik Fault
Kalakashi river
North Kunlun
Yulongkashi river
Tam Karaul Fault
South Kunlun
Kangxiwa
Karakax Fault
Kashitashi
15YK02
15YK01
Tianshuihai—Songpan-Ganzi
Karakorum—Qiangtang
Pal
Mes
Pt
PreC
Q2-4
Q1
N
E
Tianshan
Alai valley
Kashgar
Main Pamir Thrust
Tarim Basin
North Pamir
Tanymas Suture
Central Pamir
Rushan-Pshart Suture
Tajik Basin
South Pamir
Hindu Kush
Karakoram
Hotan
N. Kunlun
S. Kunlun
Karakoram Thrust
Main Kohistan Arc
Ladakh Arc
Karakoram fault
Tianshuihai—Songpan-Ganzi
Qiangtang terrane
Kabul block
Islamabad
Main Boundary Thrust
Lhasa terrane
100 km
Map Symbols:
Conformable contact
Unconformable contact
Fault
Measured section
Sections in this study
Petrography
226 Ma Published plutonic zircon U-Pb age
Compiled data in Fig. 14
Stratigraphic units in figure A:
Q2-4 Middle Pleist -Holocene
Q1 Early Pleistocene
N Neogene
E Paleogene
Mes Mesozoic
Pal Paleozoic
Pt Precambrian
J Yarkand Group
Igneous units in figure A:
Quaternary
K Cretaceous
J Jurassic
T Triassic
P Permian
C Carboniferous
S Silurian
O Ordovician
Cambrian
PreC Precambrian
Stratigraphic units in figure C:
Q Quaternary
P Pusige Fm.
E1-2 Kashi Group
C Carboniferous
Wusu Gp.= Quaternary
Xiyu Fm., original age=Quaternary, revised age=Miocene
Atushi Fm., original age=Pliocene, revised age=late Oligocene
Pakabulake Fm., original age=Miocene, revised age=middle Oligocene
Anjuan Fm., original age=Miocene, revised age=early-middle Oligocene
Keziluoyi Fm., original age=Oliocene-Miocene, revised age=early Oligocene
Wuqia Gp.= Keziluoyi, Anjuan and Pakabulake Formations
79°57′
80°00′
80°03′
36°22′
36°18′
Carboniferous
Pusige Fm.
Kashi G.
20°
10°
0 1 km
Yarkand G.
Keziluoyi Fm.
Anjuan Fm.
Pakabulake Fm.
Atushi Fm.
Kuergake
13°
14°
Quaternary
Wusu Group
Xiyu Formation, conglomerate and siltstone
Xiyu Formation, conglomerate
Modern fluvial deposit
Atushi Formation
Wuqia Group
Section starting point
Lowest conglomerates
Uppermost sandstones
End of section
0 500 m
68°
79°
24°
21°

Fig. 2

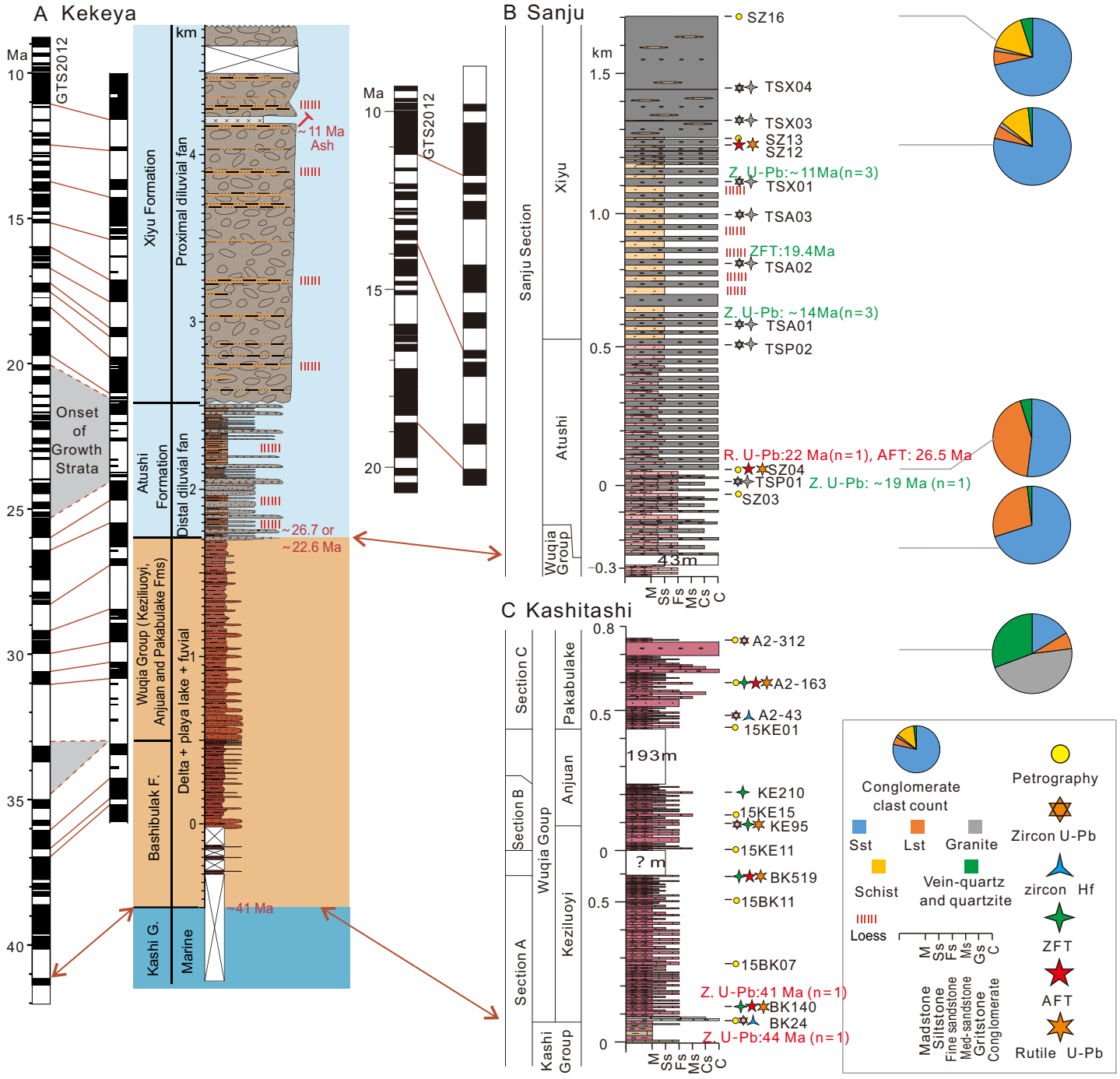
A Kekeya
B Sanju
C Kashitashi
Ma
GTS2012
km
Xiyu Formation
Proximal diluvial fan
Atushi Formation
Distal diluvial fan
Wuqia Group (Keziliuoyi, Anjuan and Pakabulake Fms)
Bashibulak F.
Delta + playa lake + fuvial
Kashi G.
Marine
Onset of Growth Strata
~11 Ma Ash
~26.7 or ~22.6 Ma
~41 Ma
Sanju Section
Xiyu
Atushi
Wuqia Group
SZ16
TSX04
TSX03
SZ13
SZ12
Z. U-Pb:~11Ma(n=3)
TSX01
TSA03
ZFT:19.4Ma
TSA02
Z. U-Pb: ~14Ma(n=3)
TSA01
TSP02
R. U-Pb:22 Ma(n=1), AFT: 26.5 Ma
SZ04
TSP01 Z. U-Pb: ~19 Ma (n=1)
SZ03
43m
Section C
Section B
Section A
Pakabulake
Anjuan
Keziluoyi
Kashi Group
A2-312
A2-163
A2-43
15KE01
193m
KE210
15KE15
KE95
15KE11
? m
BK519
15BK11
15BK07
Z. U-Pb:41 Ma (n=1)
BK140
BK24
Z. U-Pb:44 Ma (n=1)
M Ss Fs Ms Cs C
Conglomerate clast count
Sst
Lst
Granite
Schist
Vein-quartz and quartzite
Loess
Petrography
Zircon U-Pb
zircon Hf
ZFT
AFT
Rutile U-Pb
Madstone
Siltstone
Fine sandstone
Med.-sandstone
Gritstone
Conglomerate

Fig.3

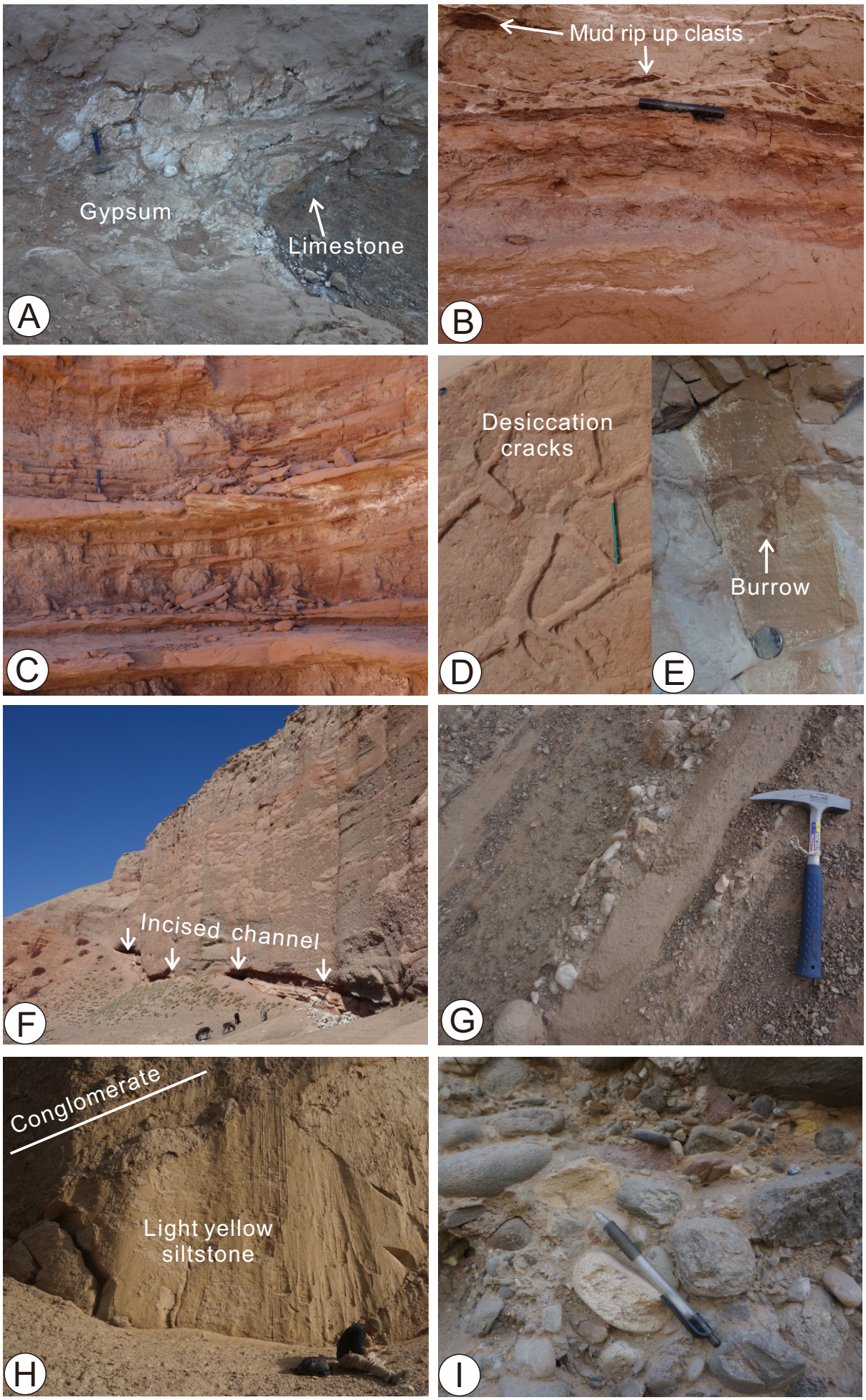
Gypsum
Limestone
A
Mud rip up clasts
B
C
Desiccation cracks
D
Burrow
E
Incised channel
F
G
Conglomerate
Light yellow siltstone
H
I

Fig. 4

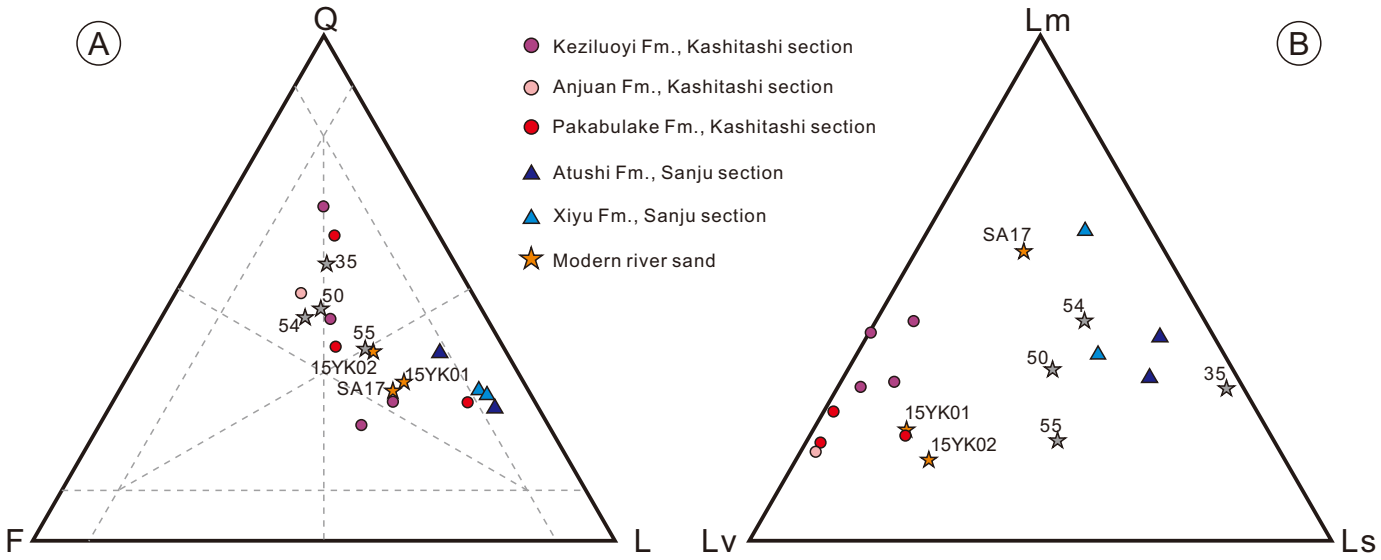
A
Q
F
L
35
50
54
55
15YK02
SA17
15YK01
Keziluoyi Fm., Kashitashi section
Anjuan Fm., Kashitashi section
Pakabulake Fm., Kashitashi section
Atushi Fm., Sanju section
Xiyu Fm., Sanju section
Modern river sand
B
Lm
Lv
Ls
SA17
54
50
35
15YK01
55
15YK02

Fig. 5

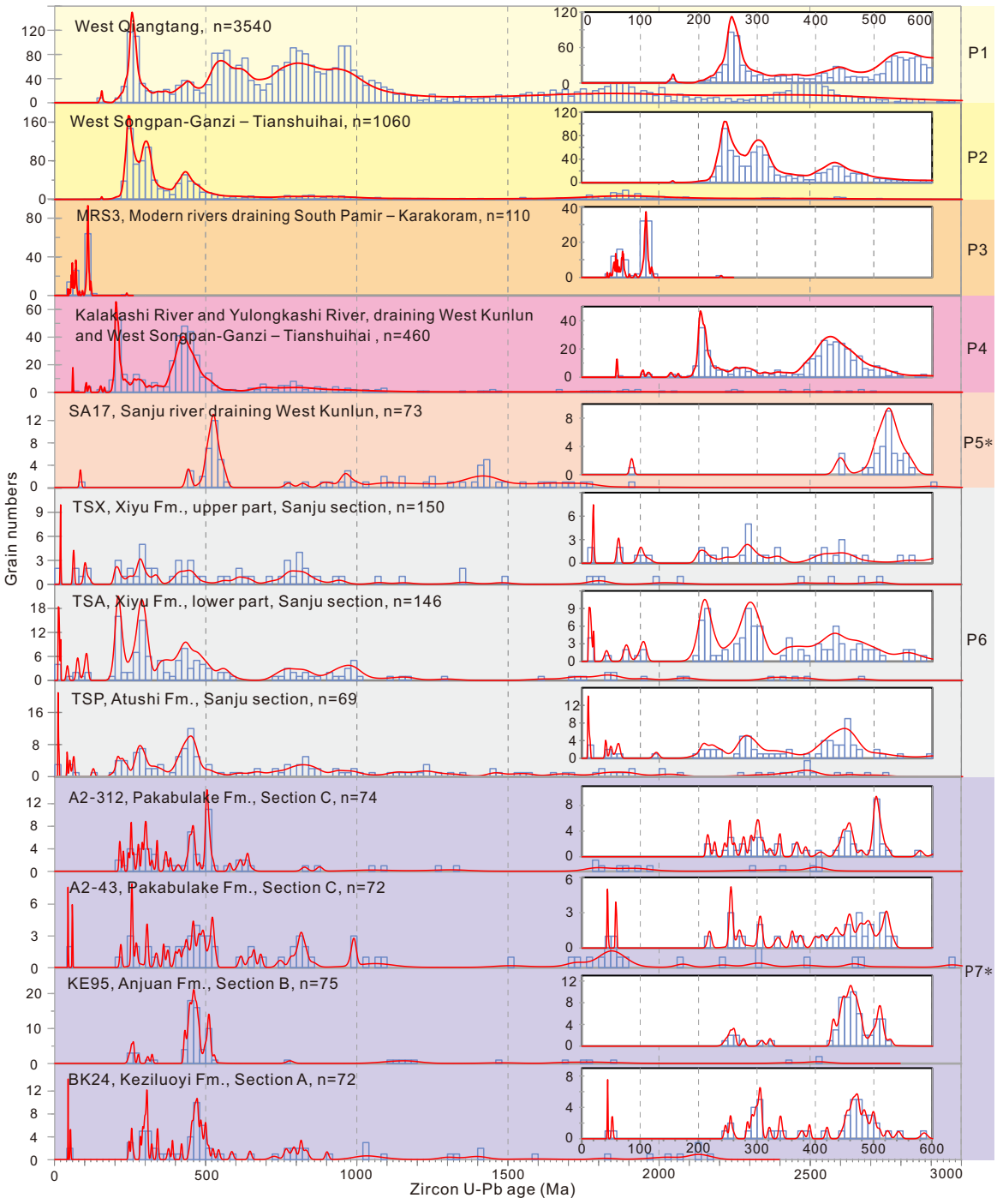
West Qiangtang, n=3540
West Songpan-Ganzi – Tianshuihai, n=1060
MRS3, Modern rivers draining South Pamir – Karakoram, n=110
Kalakashi River and Yulongkashi River, draining West Kunlun and West Songpan-Ganzi – Tianshuihai , n=460
SA17, Sanju river draining West Kunlun, n=73
TSX, Xiyu Fm., upper part, Sanju section, n=150
TSA, Xiyu Fm., lower part, Sanju section, n=146
TSP, Atushi Fm., Sanju section, n=69
A2-312, Pakabulake Fm., Section C, n=74
A2-43, Pakabulake Fm., Section C, n=72
KE95, Anjuan Fm., Section B, n=75
BK24, Keziluoyi Fm., Section A, n=72
P1
P2
P3
P4
P5*
P6
P7*
Grain numbers
Zircon U-Pb age (Ma)

Fig. 6

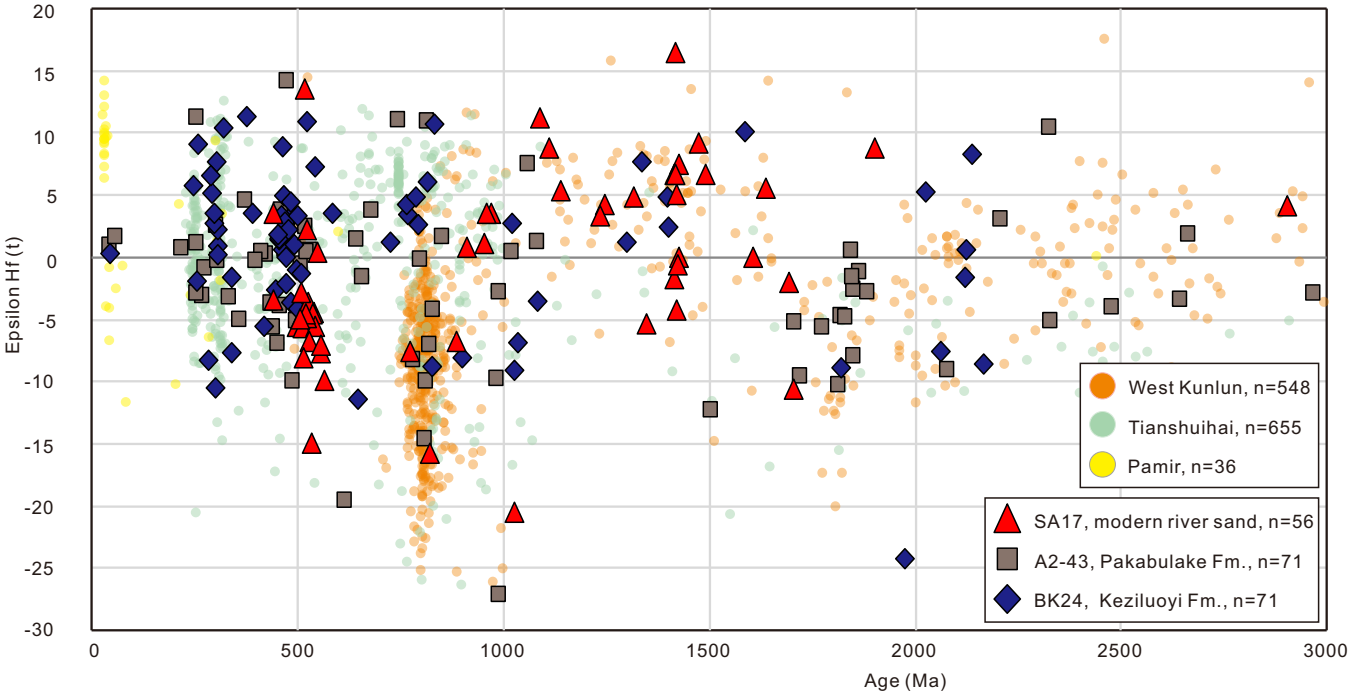
Epsilon Hf (t)
20
15
10
5
0
-5
-10
-15
-20
-25
-30
0
500
1000
1500
2000
2500
3000
Age (Ma)
West Kunlun, n=548
Tianshuihai, n=655
Pamir, n=36
SA17, modern river sand, n=56
A2-43, Pakabulake Fm., n=71
BK24, Keziluoyi Fm., n=71

Fig. 7

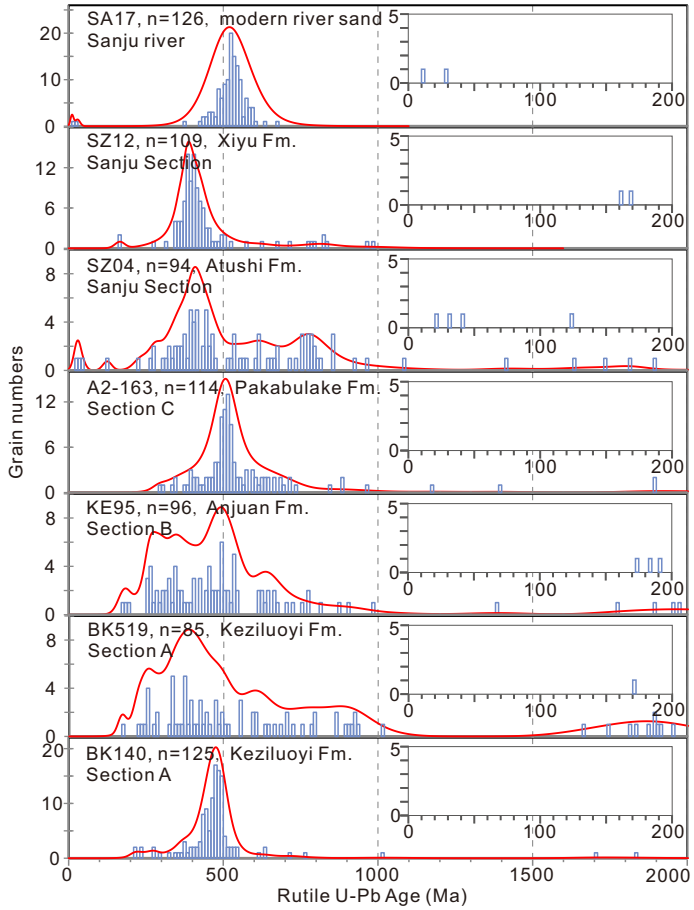
SA17, n=126, modern river sand
Sanju river
SZ12, n=109, Xiyu Fm.
Sanju Section
SZ04, n=94, Atushi Fm.
Sanju Section
A2-163, n=114, Pakabulake Fm.
Section C
KE95, n=96, Anjuan Fm.
Section B
BK519, n=85, Keziluoyi Fm.
Section A
BK140, n=125, Keziluoyi Fm.
Section A
Grain numbers
Rutile U-Pb Age (Ma)

Fig. 8

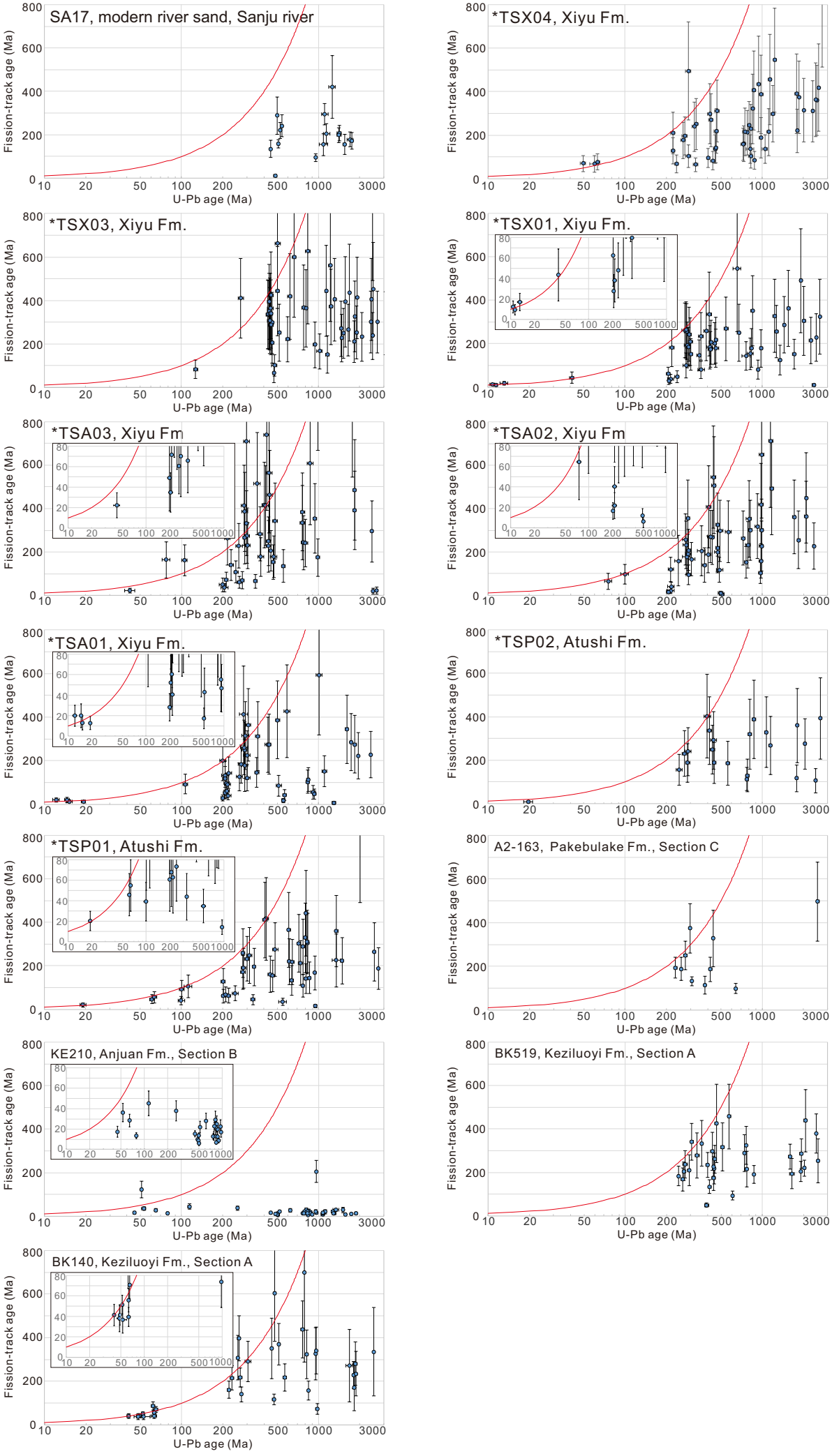
SA17, modern river sand, Sanju river
*TSX04, Xiyu Fm.
*TSX03, Xiyu Fm.
*TSX01, Xiyu Fm.
*TSA03, Xiyu Fm
*TSA02, Xiyu Fm
*TSA01, Xiyu Fm.
*TSP02, Atushi Fm.
*TSP01, Atushi Fm.
A2-163, Pakebulake Fm., Section C
KE210, Anjuan Fm., Section B
BK519, Keziluoyi Fm., Section A
BK140, Keziluoyi Fm., Section A
Fission-track age (Ma)
U-Pb age (Ma)

Fig. 9

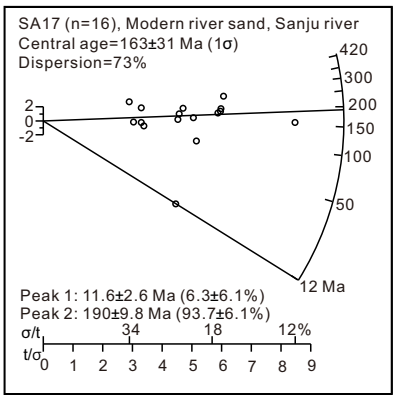
SA17 (n=16), Modern river sand, Sanju river
Central age=163±31 Ma (1σ)
Dispersion=73%
Peak 1: 11.6±2.6 Ma (6.3±6.1%)
Peak 2: 190±9.8 Ma (93.7±6.1%)
σ/t
t/σ
12 Ma

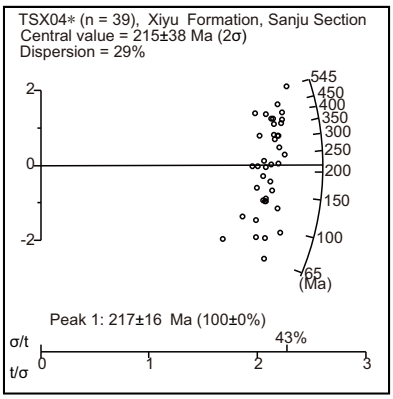
TSX04* (n = 39), Xiyu Formation, Sanju Section
Central value = 215±38 Ma (2σ)
Dispersion = 29%
Peak 1: 217±16 Ma (100±0%)
σ/t
t/σ
(Ma)

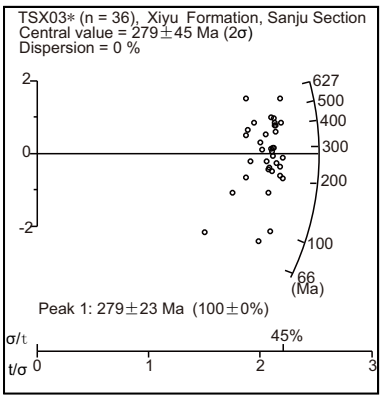
TSX03* (n = 36), Xiyu Formation, Sanju Section
Central value = 279±45 Ma (2σ)
Dispersion = 0 %
Peak 1: 279±23 Ma (100±0%)
σ/t
t/σ
(Ma)

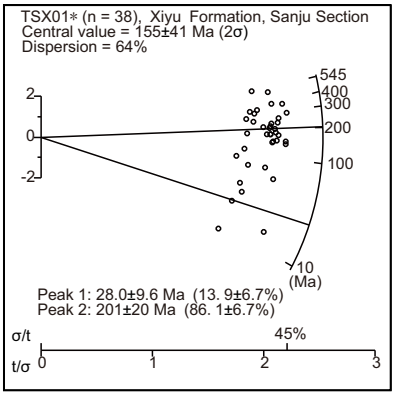
TSX01* (n = 38), Xiyu Formation, Sanju Section
Central value = 155±41 Ma (2σ)
Dispersion = 64%
Peak 1: 28.0±9.6 Ma (13. 9±6.7%)
Peak 2: 201±20 Ma (86. 1±6.7%)
σ/t
t/σ
(Ma)

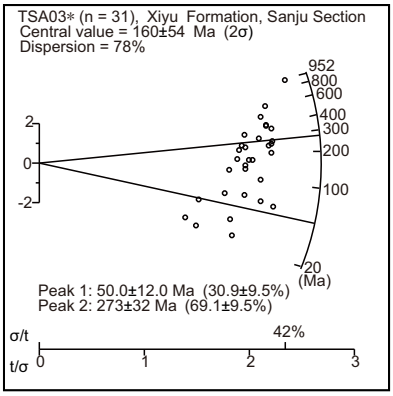
TSA03* (n = 31), Xiyu Formation, Sanju Section
Central value = 160±54 Ma (2σ)
Dispersion = 78%
Peak 1: 50.0±12.0 Ma (30.9±9.5%)
Peak 2: 273±32 Ma (69.1±9.5%)
σ/t
t/σ
(Ma)

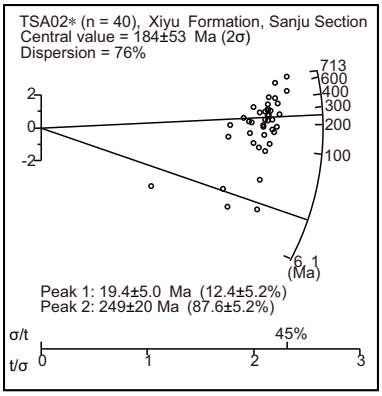
TSA02* (n = 40), Xiyu Formation, Sanju Section
Central value = 184±53 Ma (2σ)
Dispersion = 76%
Peak 1: 19.4±5.0 Ma (12.4±5.2%)
Peak 2: 249±20 Ma (87.6±5.2%)
σ/t
t/σ
(Ma)

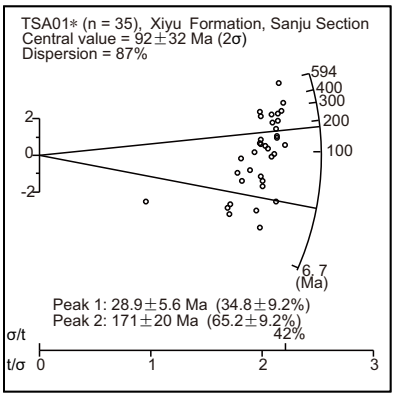
TSA01* (n = 35), Xiyu Formation, Sanju Section
Central value = 92±32 Ma (2σ)
Dispersion = 87%
Peak 1: 28.9±5.6 Ma (34.8±9.2%)
Peak 2: 171±20 Ma (65.2±9.2%)
σ/t
t/σ
(Ma)

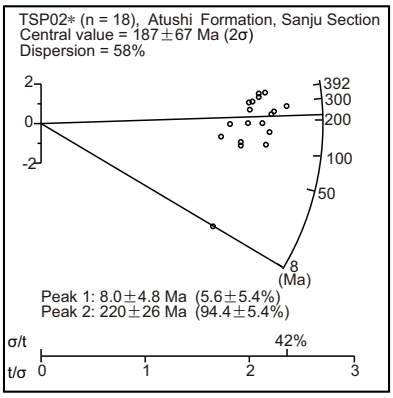
TSP02* (n = 18), Atushi Formation, Sanju Section
Central value = 187±67 Ma (2σ)
Dispersion = 58%
Peak 1: 8.0±4.8 Ma (5.6±5.4%)
Peak 2: 220±26 Ma (94.4±5.4%)
σ/t
t/σ
(Ma)

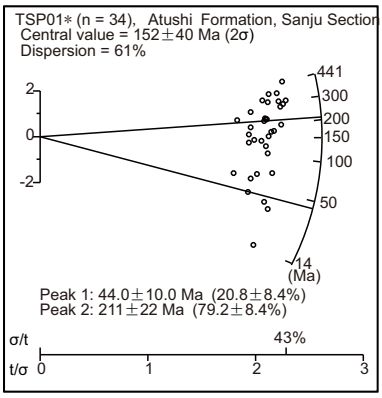
TSP01* (n = 34), Atushi Formation, Sanju Section
Central value = 152±40 Ma (2σ)
Dispersion = 61%
Peak 1: 44.0±10.0 Ma (20.8±8.4%)
Peak 2: 211±22 Ma (79.2±8.4%)
σ/t
t/σ
(Ma)

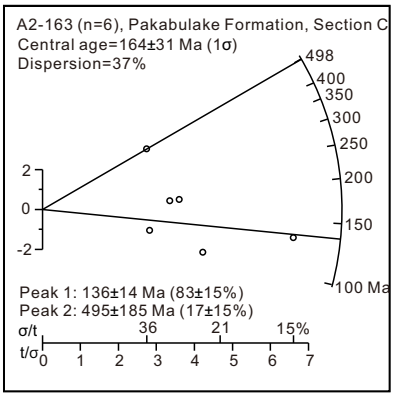
A2-163 (n=6), Pakabulake Formation, Section C
Central age=164±31 Ma (1σ)
Dispersion=37%
Peak 1: 136±14 Ma (83±15%)
Peak 2: 495±185 Ma (17±15%)
σ/t
t/σ
100 Ma

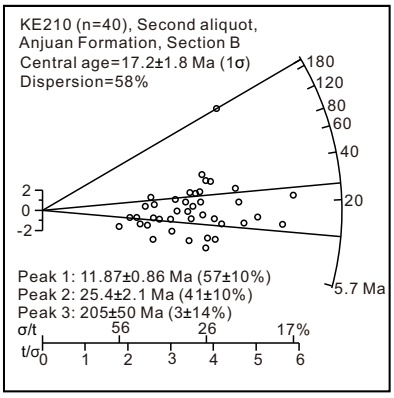
KE210 (n=40), Second aliquot,
Anjuan Formation, Section B
Central age=17.2±1.8 Ma (1σ)
Dispersion=58%
Peak 1: 11.87±0.86 Ma (57±10%)
Peak 2: 25.4±2.1 Ma (41±10%)
Peak 3: 205±50 Ma (3±14%)
σ/t
t/σ
5.7 Ma

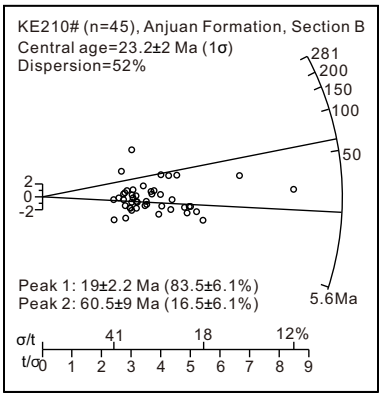
KE210# (n=45), Anjuan Formation, Section B
Central age=23.2±2 Ma (1σ)
Dispersion=52%
Peak 1: 19±2.2 Ma (83.5±6.1%)
Peak 2: 60.5±9 Ma (16.5±6.1%)
σ/t
t/σ
5.6Ma

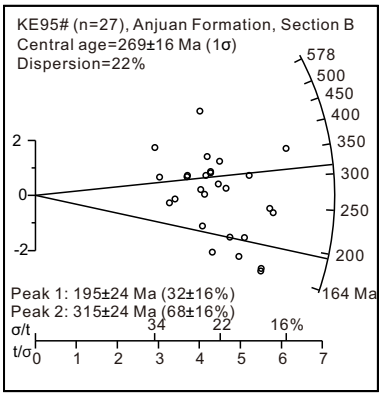
KE95# (n=27), Anjuan Formation, Section B
Central age=269±16 Ma (1σ)
Dispersion=22%
Peak 1: 195±24 Ma (32±16%)
Peak 2: 315±24 Ma (68±16%)
σ/t
t/σ
164 Ma

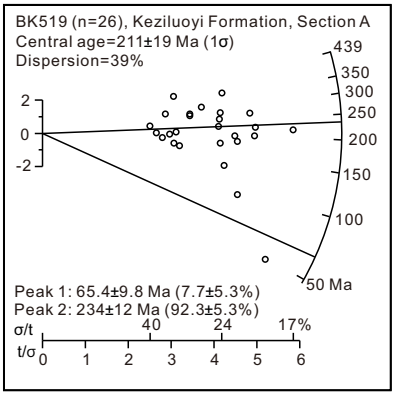
BK519 (n=26), Keziluoyi Formation, Section A
Central age=211±19 Ma (1σ)
Dispersion=39%
Peak 1: 65.4±9.8 Ma (7.7±5.3%)
Peak 2: 234±12 Ma (92.3±5.3%)
σ/t
t/σ
50 Ma

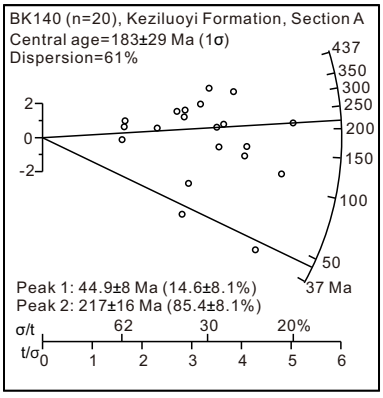
BK140 (n=20), Keziluoyi Formation, Section A
Central age=183±29 Ma (1σ)
Dispersion=61%
Peak 1: 44.9±8 Ma (14.6±8.1%)
Peak 2: 217±16 Ma (85.4±8.1%)
σ/t
t/σ
37 Ma

Fig. 10

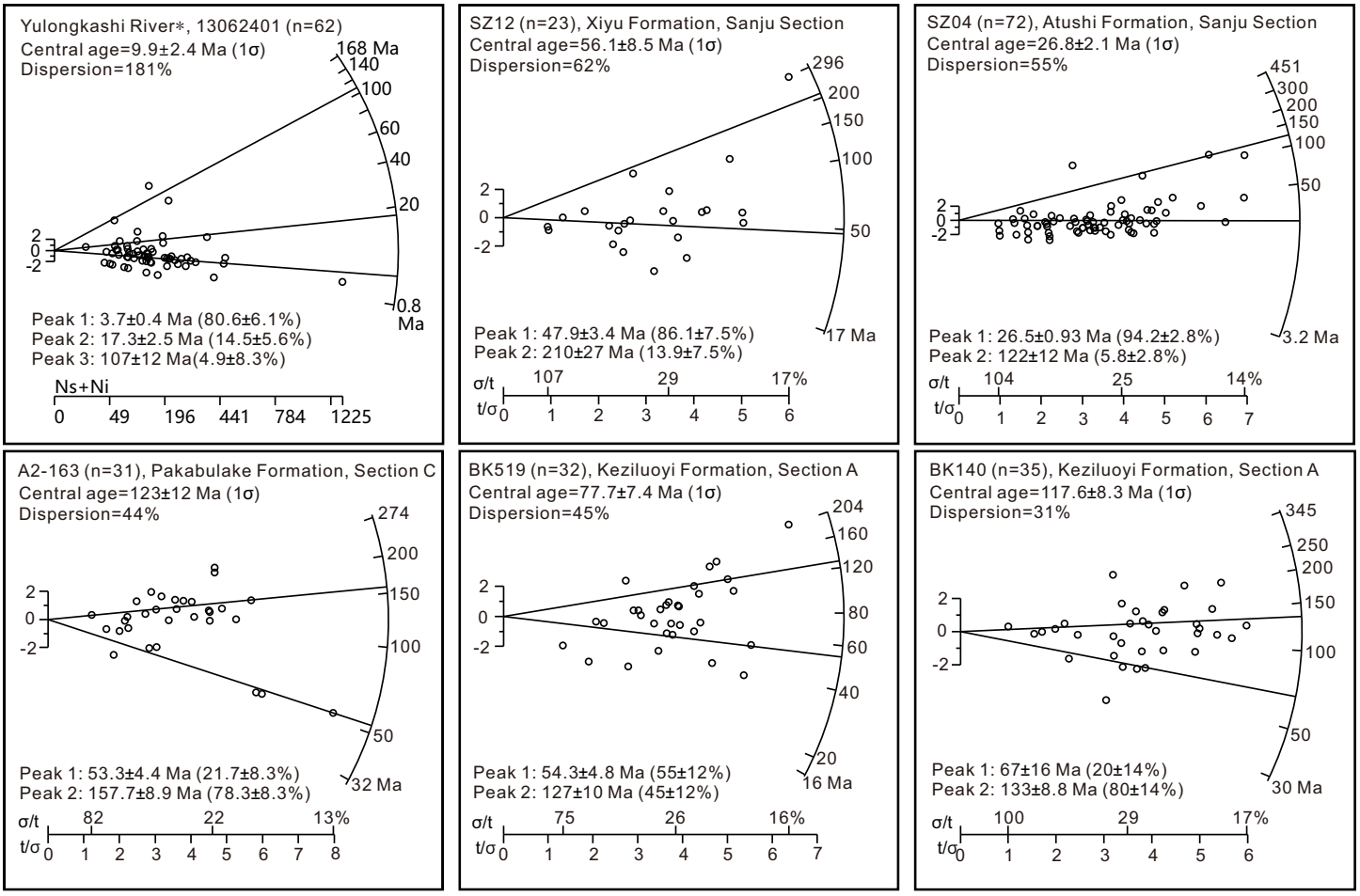
Yulongkashi River*, 13062401 (n=62)
Central age=9.9±2.4 Ma (1σ)
Dispersion=181%
168 Ma
140
100
60
40
20
0.8
Ma
2
0
-2
Peak 1: 3.7±0.4 Ma (80.6±6.1%)
Peak 2: 17.3±2.5 Ma (14.5±5.6%)
Peak 3: 107±12 Ma(4.9±8.3%)
Ns+Ni
0 49 196 441 784 1225
SZ12 (n=23), Xiyu Formation, Sanju Section
Central age=56.1±8.5 Ma (1σ)
Dispersion=62%
296
200
150
100
50
17 Ma
Peak 1: 47.9±3.4 Ma (86.1±7.5%)
Peak 2: 210±27 Ma (13.9±7.5%)
σ/t 107 29 17%
t/σ 0 1 2 3 4 5 6
SZ04 (n=72), Atushi Formation, Sanju Section
Central age=26.8±2.1 Ma (1σ)
Dispersion=55%
451
300
200
150
100
50
3.2 Ma
Peak 1: 26.5±0.93 Ma (94.2±2.8%)
Peak 2: 122±12 Ma (5.8±2.8%)
σ/t 104 25 14%
t/σ 0 1 2 3 4 5 6 7
A2-163 (n=31), Pakabulake Formation, Section C
Central age=123±12 Ma (1σ)
Dispersion=44%
274
200
150
100
50
32 Ma
Peak 1: 53.3±4.4 Ma (21.7±8.3%)
Peak 2: 157.7±8.9 Ma (78.3±8.3%)
σ/t 82 22 13%
t/σ 0 1 2 3 4 5 6 7 8
BK519 (n=32), Keziluoyi Formation, Section A
Central age=77.7±7.4 Ma (1σ)
Dispersion=45%
204
160
120
80
60
40
20
16 Ma
Peak 1: 54.3±4.8 Ma (55±12%)
Peak 2: 127±10 Ma (45±12%)
σ/t 75 26 16%
t/σ 0 1 2 3 4 5 6 7
BK140 (n=35), Keziluoyi Formation, Section A
Central age=117.6±8.3 Ma (1σ)
Dispersion=31%
345
250
200
150
100
50
30 Ma
Peak 1: 67±16 Ma (20±14%)
Peak 2: 133±8.8 Ma (80±14%)
σ/t 100 29 17%
t/σ 0 1 2 3 4 5 6

Fig. 11

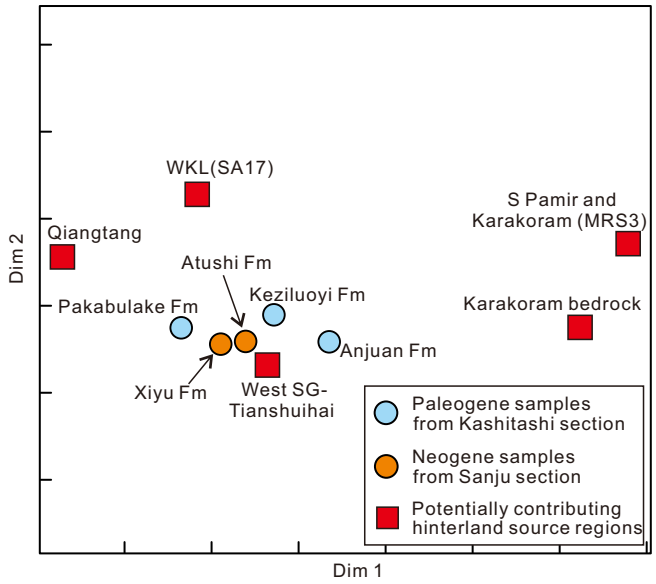
WKL(SA17)
S Pamir and
Karakoram (MRS3)
Qiangtang
Atushi Fm
Keziluoyi Fm
Pakabulake Fm
Karakoram bedrock
Anjuan Fm
Xiyu Fm
West SG-
Tianshuihai
Paleogene samples
from Kashitashi section
Neogene samples
from Sanju section
Potentially contributing
hinterland source regions
Dim 2
Dim 1

Fig. 12

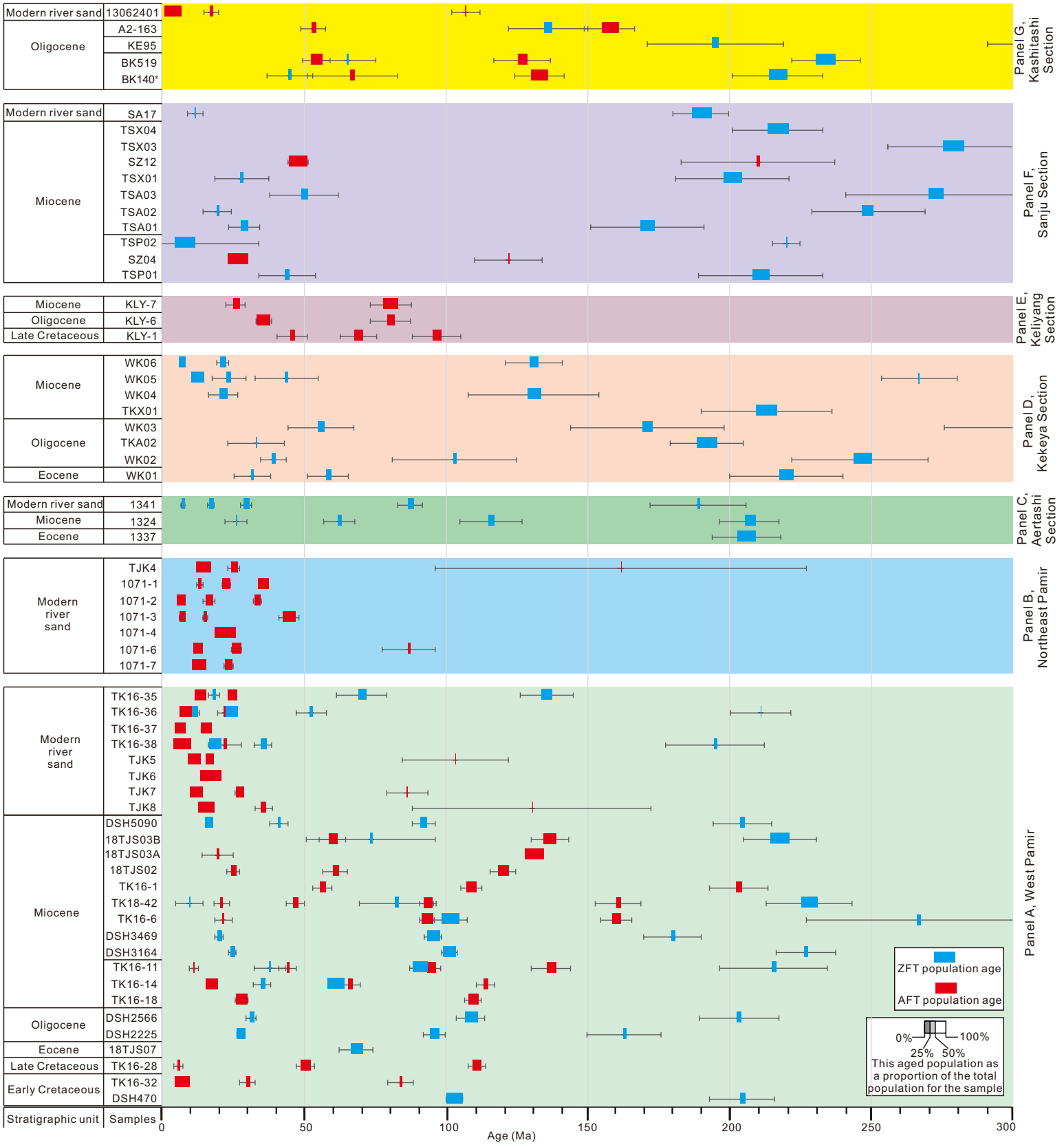
Modern river sand
13062401
Oligocene
A2-163
KE95
BK519
BK140*
Panel G, Kashitashi Section
Modern river sand
SA17
Miocene
TSX04
TSX03
SZ12
TSX01
TSA03
TSA02
TSA01
TSP02
SZ04
TSP01
Panel F, Sanju Section
Miocene
KLY-7
Oligocene
KLY-6
Late Cretaceous
KLY-1
Panel E, Keliyang Section
Miocene
WK06
WK05
WK04
TKX01
Oligocene
WK03
TKA02
WK02
Eocene
WK01
Panel D, Kekeya Section
Modern river sand
1341
Miocene
1324
Eocene
1337
Panel C, Aertashi Section
Modern river sand
TJK4
1071-1
1071-2
1071-3
1071-4
1071-6
1071-7
Panel B, Northeast Pamir
Modern river sand
TK16-35
TK16-36
TK16-37
TK16-38
TJK5
TJK6
TJK7
TJK8
Miocene
DSH5090
18TJS03B
18TJS03A
18TJS02
TK16-1
TK18-42
TK16-6
DSH3469
DSH3164
TK16-11
TK16-14
TK16-18
Oligocene
DSH2566
DSH2225
Eocene
18TJS07
Late Cretaceous
TK16-28
Early Cretaceous
TK16-32
DSH470
ZFT population age
AFT population age
0%
100%
25%
50%
This aged population as a proportion of the total population for the sample
Panel A, West Pamir
Stratigraphic unit
Samples
0
50
100
150
200
250
300
Age (Ma)